1   **Proposed New Dry and Hybrid Concrete Joints with GFRP Bolts and GFRP**

2   **Reinforcement under Cyclic Loading: Testing and Analysis**

3   Tuan T. Ngo[1], Thong M. Pham[2]*, Hong Hao[3]*, Wensu Chen[4], and Ngoc San Ha[5]

4   **Abstract**

5   This study proposes a new hybrid concrete joint using glass fibre reinforced polymer (GFRP) bolts

6   and reinforcements to replace steel bolts and reinforcements for corrosion damage mitigation. The

7   experimental results indicate that the proposed hybrid concrete joints satisfy the seismic-resistant

8   requirements with respect to the ductility and energy dissipation. The energy dissipation of the hybrid

9   concrete joint was approximately 57% higher than the reference monolithic joint. In addition, the

10   application of GFRP bolts and reinforcements not only avoided brittle failure during the test but also

11   showed excellent behaviours in terms of the drift ratio, ductility, and energy dissipation. Numerical

12   simulation using ABAQUS software was also carried out, which successfully captured the failure

13   modes, drift ratios, and peak loads of the dry, hybrid, and monolithic joints. The numerical results

14   proved that the common assumptions which were adopted in the proposed models of the previous

15   studies [1, 2] were reliable to predict the peak loads. The ratio of the thickness of the concrete-end-

16   plate (CEP) over the height of the beam of 1.3 was the optimal value and it can be used in CEP design

17   of the dry joint. Finally, the developed three-dimensional finite element (3D-FE) model verified with

[1] Research Assistant, Center for Infrastructural Monitoring and Protection, School of Civil and Mechanical Engineering, Curtin University, Kent Street, Bentley, WA 6102, Australia and the Faculty of Engineering and Technology, Quy Nhon University, 170 An Duong Vuong Street, Binh Dinh, Viet Nam. Email: tangtuan.ngo@curtin.edu.au

[2] Senior Lecturer, Center for Infrastructural Monitoring and Protection, School of Civil and Mechanical Engineering, Curtin University, Kent Street, Bentley, WA 6102, Australia (Corresponding author). Email: thong.pham@curtin.edu.au

[3] John Curtin Distinguished Professor, Center for Infrastructural Monitoring and Protection, School of Civil and Mechanical Engineering, Curtin University, Kent Street, Bentley, WA 6102, Australia (Corresponding author). Email: hong.hao@curtin.edu.au

[4] Associate Professor, Center for Infrastructural Monitoring and Protection, School of Civil and Mechanical Engineering, Curtin University, Kent Street, Bentley, WA 6102, Australia. Email: wensu.chen@curtin.edu.au

[5] Research Fellow, Center for Infrastructural Monitoring and Protection, School of Civil and Mechanical Engineering, Curtin University, Kent Street, Bentley, WA 6102, Australia. Email: san.ha@curtin.edu.au

18   the testing data can be confidently applied in future studies to investigate the seismic performances

19   of the dry, hybrid, and monolithic beam-column joints using GFRP reinforcements and bolts.

20   **Keywords**: GFRP bolts; GFRP reinforcements; Ductile precast joints; Prestress bolts; Exterior dry

21   joints; Hybrid joints; ABAQUS.

22

1. Introduction

Beam-column joints are important components in a building since they connect beams to columns and transmit forces between these components. It was observed in many earthquakes that failures of the beam-column joints could cause collapse of the building while no damage was observed on the beams and columns [3-7]. To resolve this issue, a design method that shifts the failure from the beam-column joints to the beam-ends has been proposed in previous studies. This method helps to increase the ductility and energy dissipation (ED) and avoid brittle failure of buildings under earthquake loading [1, 3, 8]. Numerous studies [1, 2, 8, 9] indicated that to ensure the plastic hinges only occur at the beam-end, the beam-column joints need to be sufficiently strong to resist the shear failure within the joint area. Therefore, it is critical to increase the shear resistance of the joint to resist seismic loadings.

In practice, there are generally two kinds of beam-column joints, i.e., monolithic and precast joints. For precast joints, they can be classified into three groups including wet, dry, and hybrid joints. The hybrid joint is a type in between the wet and the dry joints. For dry and hybrid joints, beams and columns are erected in a construction site without the requirements of formworks. For wet joints, beams and columns are placed at designed positions using a crane, concrete needs to be filled into gaps during the construction. Accordingly, formwork is required during the concrete filling for wet joints while it is not required for hybrid joints. It is because the hybrid joints can resist loads even without the filling concrete. Nowadays, the dry and hybrid joints have been increasingly applied in many constructions considering their various advantages such as shorter construction time, reduced construction cost, easier replacement of damaged components, more convenient application of new materials and technologies (e.g., 3D printing, geopolymer concrete, ultra-high performance concrete and fibre-reinforced concrete).

46 Monolithic and wet joints are more commonly used because they have been more intensively studied

47 and show promising performances in the critical indices such as drift ratio (DR), ductility, ED and

48 load-carrying capacity. The application of the hybrid and dry joints has been avoided in the seismic-

49 prone areas owing to the lack of appropriate hybrid and dry joint types with sufficient strength and

50 limited knowledge about their behaviours under earthquake loading. To resolve these drawbacks,

51 many studies have been conducted to address this issue. Ngo, et al. [3] proposed a new dry joint using

52 CFRP bolts and concrete-end-plate (CEP). The proposed dry joints showed higher values in terms of

53 the peak load (27-61%), effective stiffness (27-55%), and ED (45-75%), compared to those of the

54 corresponding monolithic joint. All the precast joints in the latter study reached 3% drift ratio (DR)

55 which satisfied the requirements of ASCE 41-17 [10] and CSA A23.3-07 [11] for applying in seismic-

56 prone regions. In addition, an analytical model was proposed to predict the load-carrying capacity in

57 other studies [1, 2]. The variation between the experiment and the proposed analytical model was less

58 than 2% [1]. However, the bulky appearance of the CEP was a disadvantage of this dry joint which

59 needs further improvement. Alver, et al. [12] and Jin, et al. [13] investigated another dry joint using

60 steel tendons to connect beams and columns. These studies indicated that the shear failure primarily

61 governed the failure modes of the dry joint. Comparing to the dry joint using CFRP bolts and CEP

62 [2, 14], the dry joints using steel tendons face more challenges in erecting and replacing damaged

63 components because the steel tendons need to go through beams and columns. On the other hand,

64 numerical studies on the dry and hybrid joints under cyclic loading are very limited, most of previous

65 studies were based on experimental tests [15-19]. The tests, however, can only provide limited

66 measurements of the joint's performance while some critical measurements could not be obtained,

67 e.g., stress distribution in concrete and complex stress states within the joint region.

68 Numerical simulation using three-dimensional finite element (3D-FE) model was applied in various

69 studies to investigate the structural performances. The application of numerical simulation can reduce

70 the experimental costs and time for manufacturing and testing specimens. There are some software

71   packages which can be used to simulate the behaviours of structures under static and dynamic loading,

72   including ANSYS, DIANA, and ABAQUS. Nevertheless, previous numerical studies showed

73   considerable variations between experimental and numerical results. Kaya and Arslan [20] used

74   ANSYS to simulate the post-tensioned precast beam-column joints using steel tendons under various

75   prestress levels. A large difference in stiffness between experiment and numerical simulation was

76   observed in the study. Also, the hysteretic curves of the numerical simulation were not presented in

77   the previous study [20]. Alaee and Li [21] used DIANA to investigate structural responses of

78   monolithic joints using high-strength concrete and high-strength reinforcements. The 3D-FE model

79   well captured the envelope curves and predicted the peak loads. However, a high variation of the

80   hysteretic curve obtained from the experiment and numerical simulation was also recorded. In other

81   studies [22, 23], DIANA was utilized to examine the effects of the axial loads and the thickness of

82   steel plates in hybrid steel-concrete joints. These studies found that applying the axial force up to

83    $(\frac{N}{A_c f_c'}) = 0.3$ could improve the joint performances in term of the peak load. However, when

84   increasing axial load with the value of $(\frac{N}{A_c f_c'}) > 0.3$, negative effects were observed in the joint's

85   behaviours. Moreover, the thickness of the steel plate significantly affected the displacement and ED

86   of this hybrid joint, and 14-mm thickness of the steel plate was found as an optimal design for the

87   investigated joints.

88   Mosallam, et al. [24] utilised ABAQUS to investigate the retrofitted monolithic beam-column joints

89   with FRP laminates. Higher stiffness and peak load were observed for the numerical simulation

90   results, compared to the corresponding experimental results. For instance, the variation of the peak

91   loads in [24] was in a range of 9-32%. Le, et al. [25] conducted a parametric study on precast

92   segmental beams using ABAQUS to investigate the effects of prestressing levels on the beam

93   performances. The numerical results indicated that the prestressing levels governed the failure

94   patterns, peak load, and ductility. For instance, higher prestress forces could increase the peak load

95   of the precast segmental beams by approximately 20-22%. Moreover, a significant variation of the

96   initial stiffness between the numerical simulation and experiment was reported. The above studies

97   suggest that achieving a good agreement between the numerical simulation and experiment results,

98   especially the hysteretic curves under cyclic loading is challenging. This issue is attributed to a lack

99   of material models which could well simulate material performance under different loading

100 conditions. For example, the concrete damaged plasticity model in ABAQUS could not well capture

101 the shear and tensile failures of reinforced-concrete structures under cyclic loading [26, 27].

102 Therefore, in many previous studies, only monotonic loading was considered to get the load-

103 displacement relationship, instead of modelling the performance under cyclic loading in using

104 ABAQUS [7, 28, 29]. In addition, running a simulation of the beam-column joints under cyclic

105 loading requires a high computational cost compared to monotonic loading.

106 This study reports a part of a bigger project focusing on proposing and investigating new precast

107 joints which could effectively resolve corrosion problem, reduce construction cost, enhance structural

108 resilience and sustainability, and satisfy the requirement for collapse prevention performance level

109 under high levels of earthquake loading. There are four innovations in this study, compared to

110 previous studies [1-3]. (1) A new hybrid joint was proposed to resolve a disadvantage related to the

111 bulky appearance of the dry joint with the CEP. Together with the dry joint proposed in the previous

112 studies [1-3], this new hybrid join offers a new option of consideration to engineers in designing

113 precast joints. (2) GFRP reinforcements and bolts were used to replace steel reinforcements and bolts

114 for effective mitigation of the corrosion problem of precast joints. It is noted that there have been no

115 studies of the performances of precast joints with GFRP reinforcements and bolts under cyclic loading

116 in open literature yet. (3) Numerical model was build using ABAQUS to investigate the structural

117 responses of the dry and hybrid joints with CEP and bolts under both cyclic and monotonic loads.

118 Based on the numerical simulation, some parameters (e.g. shear stress distribution in the concrete of

119 CEP and principal stress flow), which could not be straightforwardly measured in the experiment,

120 will be discussed in this study. In addition, the assumptions in the previously proposed model to

121 predict the load-carrying capacity [1, 2] were validated, based on the numerical simulation results.

122 (4) The CEP thickness in both the dry and hybrid joints is the critical parameter of these joints and

123 thus the effects of the CEP thickness were examined by using experimental and numerical results.

124 **2. Experimental program**

125 This study investigates the performances of a newly proposed hybrid joint using GFRP bolts, GFRP

126 reinforcements, and concrete-end-plate (CEP). The thickness of the CEP, which is the critical

127 parameter, was varied to examine its influence on the joints' performance. Six specimens, including

128 two monolithic joints (M1-SR and M2-GR) as references, two-hybrid joints (H3-GR-T200 and H4-

129 GR-T100), and two dry joints (D5-SR-S-T200 and D6-GR-S-T100), were cast and tested under cyclic

130 loading. The letters "M", "H", and "D" indicate the monolithic, hybrid and dry joints, respectively.

131 "GR" denotes GFRP reinforcements whereas "SR" denotes steel reinforcements. "T100" and "T200"

132 represent the thickness of CEP of 100 and 200 mm, respectively. It is noted that both the dry joints

133 used steel bolts to connect the beam and column so the letter "S" indicates steel bolts. The information

134 of all the specimens is summarized in Table 1. Details of the specimen dimensions, test setups, and

135 material properties are presented in the subsequent sections.

136 **Table 1.** Specimen design.

| Names	Joint Types	Reinforcements	Bolts	CEP thickness (mm)	CEP cross-section (mm)
M1-SR	Monolithic	Steel	-	-	-
M2-GR	Monolithic	GFRP	-	-	-
H3-GR-T200	Hybrid	GFRP	GFRP	200	200×250
H4-GR-T100	Hybrid	GFRP	GFRP	100	200×250
D5-SR-S-T200	Dry	Steel	Steel	200	150×350
D6-GR-S-T100	Dry	GFRP	Steel	100	200×350

137 Note: - = not applicable.

2.1 Details of beam-column joints

Details of the dimensions and shapes of the monolithic joints and hybrid joints are illustrated in Figs. 1 and 2. It should be noted that in the design and preparation of the specimens for testing, the experiences gained in the previous studies [1, 3], as well as in the process of the current study, were taken into consideration. Some improvements on the hybrid and dry joints were made to further ease the assembly process of beams and columns. Therefore, the dimensions of the six tested specimens were not exactly the same, and hence the results among the specimens might not be directly comparable, but indicative only and can be used to verify the numerical models. The beam width of Specimens H3-GR-T200, H4-GR-T100, and D6-GR-S-T100 were 200 mm. To ensure fair comparisons between the hybrid/dry joints and the monolithic joint, the beam width of the monolithic specimen M2-GR was also increased up to 200 mm. The beam cross-sections of Specimen M2-GR, H3-GR-T200, H4-GR-T100, and D6-GR-S-T100 were 150-mm height and 200-mm width whereas those of Specimens M1-SR and D5-SR-S-T200 were 150 and 150 mm, respectively. The beam length of all the specimens was 820 mm. The beam of the hybrid and dry joints was divided into two parts, including Beam A and the CEP (see Fig. 3). The cross-section of the CEP of hybrid and dry joints was different. The CEP cross-section of hybrid joints was 200-mm width and 250-mm height, whereas that of dry joints was 200/150-mm width and 350-mm height. In addition, due to the requirements for accommodating both bolts and nuts, the cross-section of CEP was larger than that of Beam A. As the primary parameter in this study, the thickness of CEP varied from 100 mm (Specimens H4-GR-T100, D6-GR-S-T100) to 200 mm (Specimens H3-GR-T200, D5-SR-S-T200) to investigate its effect on the performance. The dimensions of the column remained unchanged in all the specimens with 200-mm square cross-section and 1280-mm length. The diameter of the GFRP longitudinal rebars and GFRP stirrups was 17.1 mm and 10.5 mm, respectively. For convenience, GFRP spiral stirrups were applied in both the beam and column with the same spacing of 35 mm, as shown in Fig. 1.
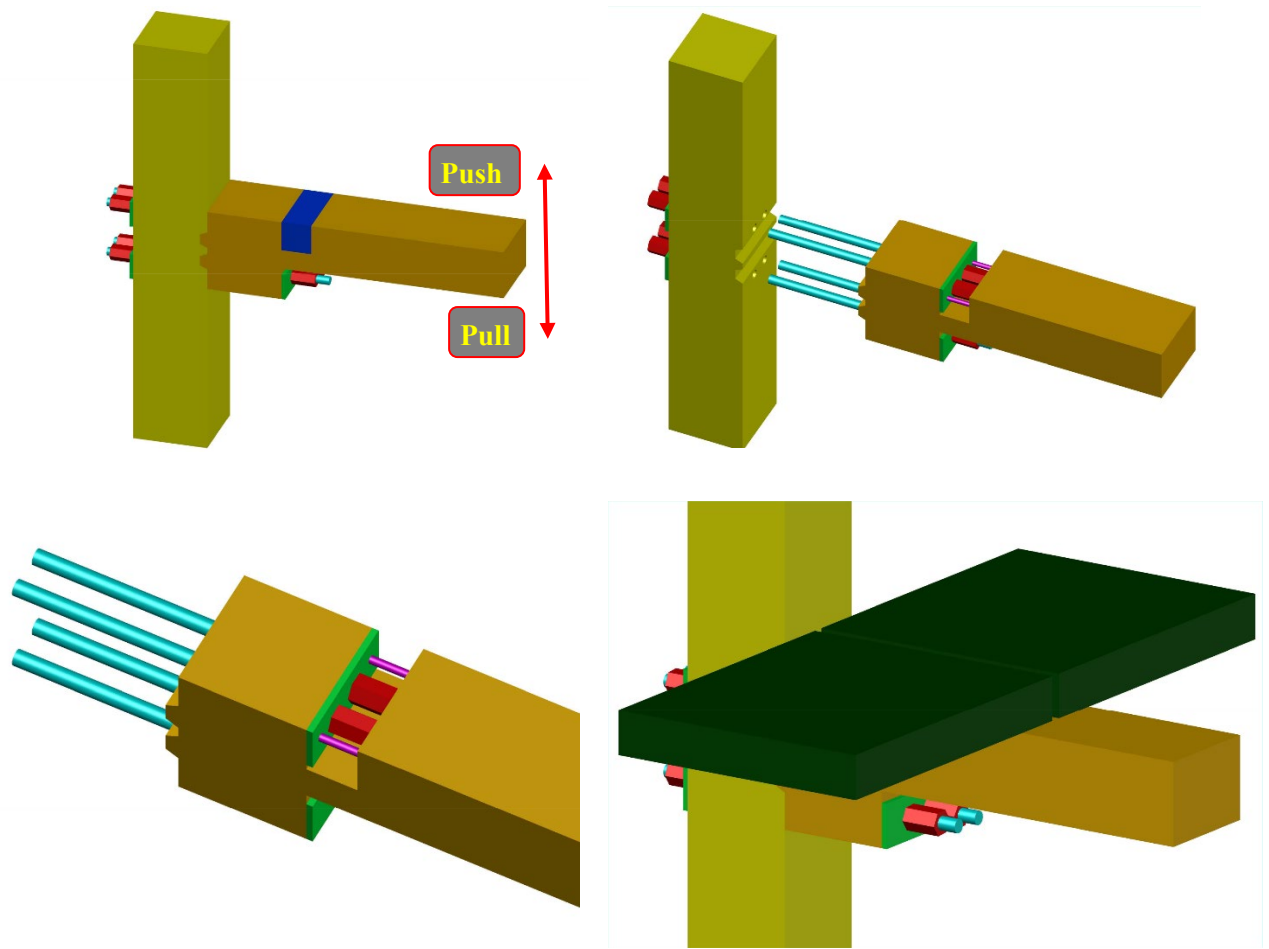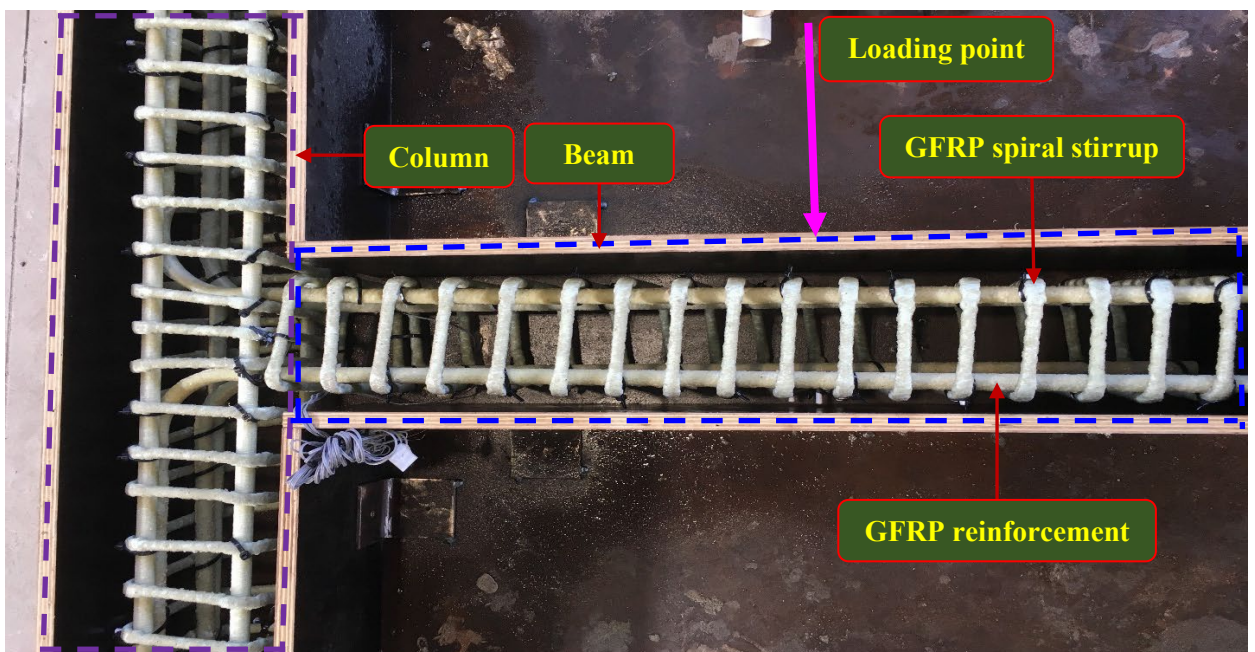
163

164
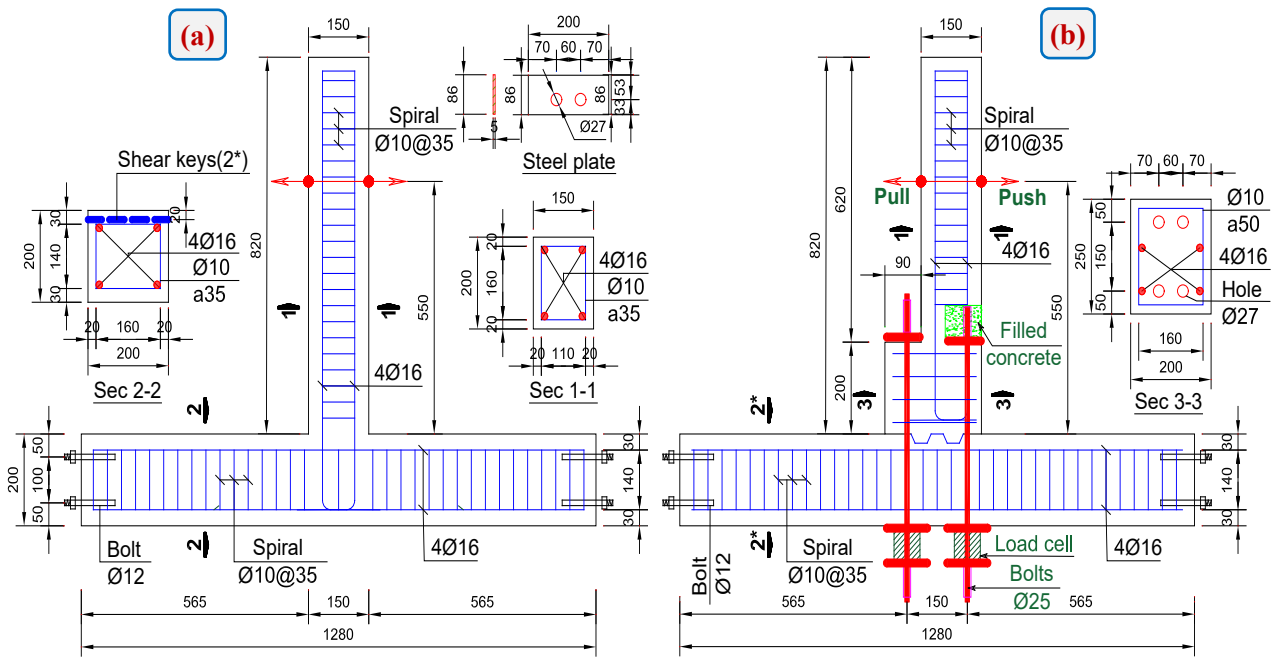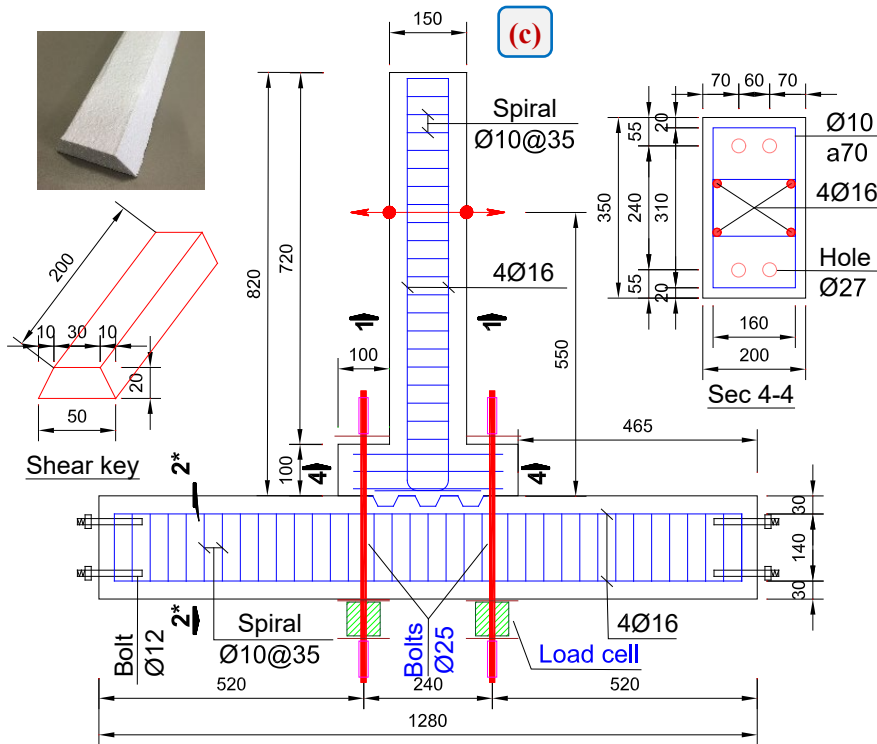
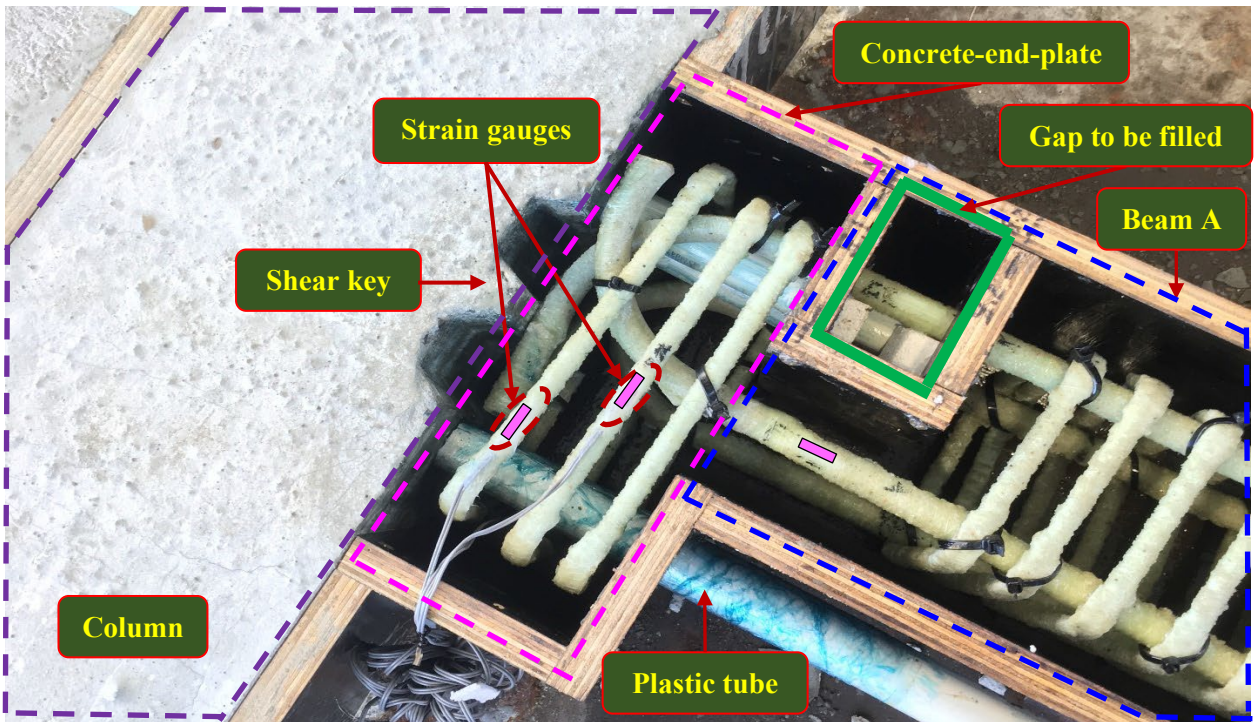**Fig. 1.** Dimensions of the (a) monolithic joint, (b) hybrid joint, and (c) dry joint (unit: mm).

166

Push

Pull

Fig. 2. 3D-views of the newly proposed hybrid joint.

167

Fig. 3. Details of reinforcements, shear keys, and formworks.

Fig. 3 shows a typical view of GFRP cages, formworks, and shear keys. Foam moulds were attached to the timber plates by using a silicone sealant to form the shear keys on the columns. The columns with the shear keys were cast first and then they were used as the formworks to cast the beams. This method ensures that the surfaces of the shear keys on the beam and column were properly fitted after

173 casting. To ensure that the beams and columns could be separated after casting, grease was used to

174 sweep on the column and shear key surfaces before casting the beams. High strength concrete was

175 filled into the green gap (see Fig. 3) after applying prestress forces to the GFRP bolts. In practice,

176 two timber plates can be fixed at both sides of the gaps and then high strength concrete is filled easily

177 on the top of the gaps. Four GFRP bolts with a diameter of 25 mm were used to connect the beam to

178 the column before the test. These GFRP bolts were applied a high prestress force up to 35 kN by the

179 use of a hydraulic jack, chair, and spanner [30]. This new method of being able to apply high prestress

180 force to FRP bolts was described in [30], which effectively resolved the limitations in the previous

181 studies [3, 14] of not being able to apply large prestress force to FRP bolts owing to the weak shear

182 strength of FRP material [1-3] (see Fig. 4). The conventional method of using a torch wrench to apply

183 the prestress force to CFRP bolts caused local damage at the nut location. As a result, only 6.5-10.5

184 kN of the prestress force was applied to CFRP bolts due to the low torsion resistance of the bolts in

185 the previous studies [1-3].
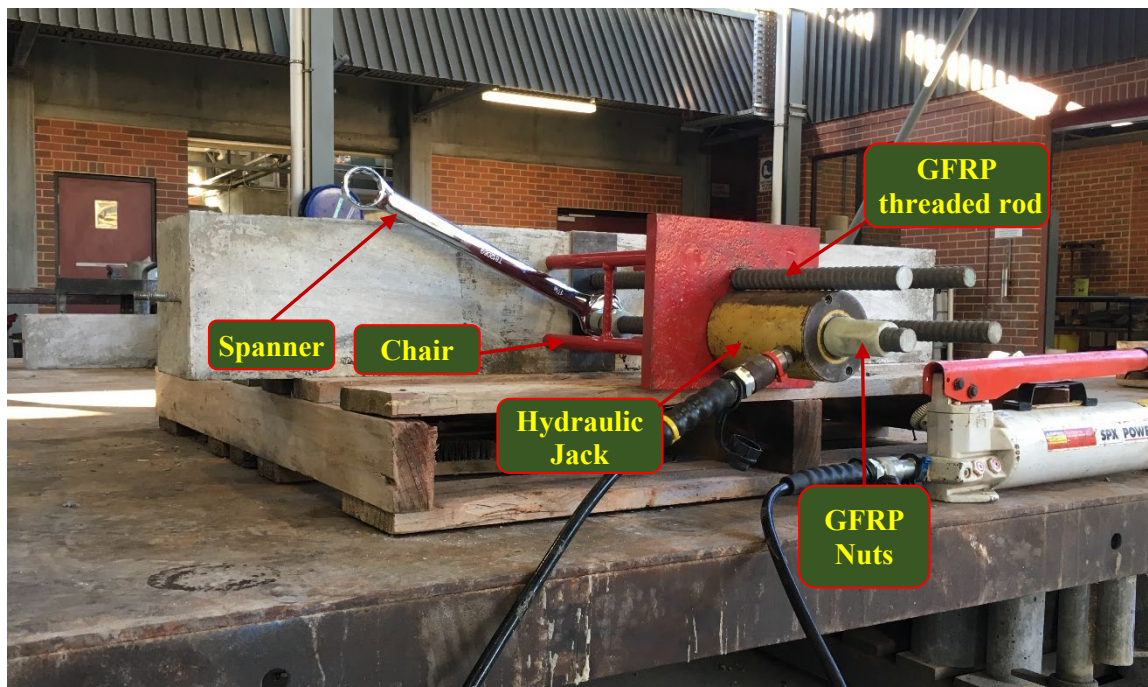
186

187 **Fig. 4.** Setup for applying prestress to GFRP bolts.

188 **2.2 Test setups**

189 Fig. 5 shows a typical test setup of the hybrid joints. Before testing, a prestress force of 35 kN was

190 applied to each GFRP bolt. A 500-kN hydraulic jack was used to apply the cyclic load at the loading

191 point, 550 mm from the column surface. Another hydraulic jack was placed on the column top to

192 apply 65 kN ($\approx$ 0.03 $A_c f_c$) axial force on the column (see Fig. 5). This axial force was maintained as

193 low as possible to simulate the most unfavourable case of joint behaviours. Four load cells with a

194 capacity of 200 kN were used to monitor the cyclic loading, the tensile forces in the bolts, and axial

195 forces in the column during the tests as shown in Fig. 5. Strain of the reinforcements was measured

196 by 5-mm strain gauges. The typical loading history (see Fig. 6) was based on ACI T1.1-01 [31]

197 standard and the previous studies [1, 3]. Due to the time restraint, two fully reversed cycles were

198 conducted for each drift ratio under displacement control at the levels of 6–9 mm/min. The beam-

199 column joints were tested until 85% post-peak load. The test could be stopped before or after 9% DR

200 which depended on the joint capacity.
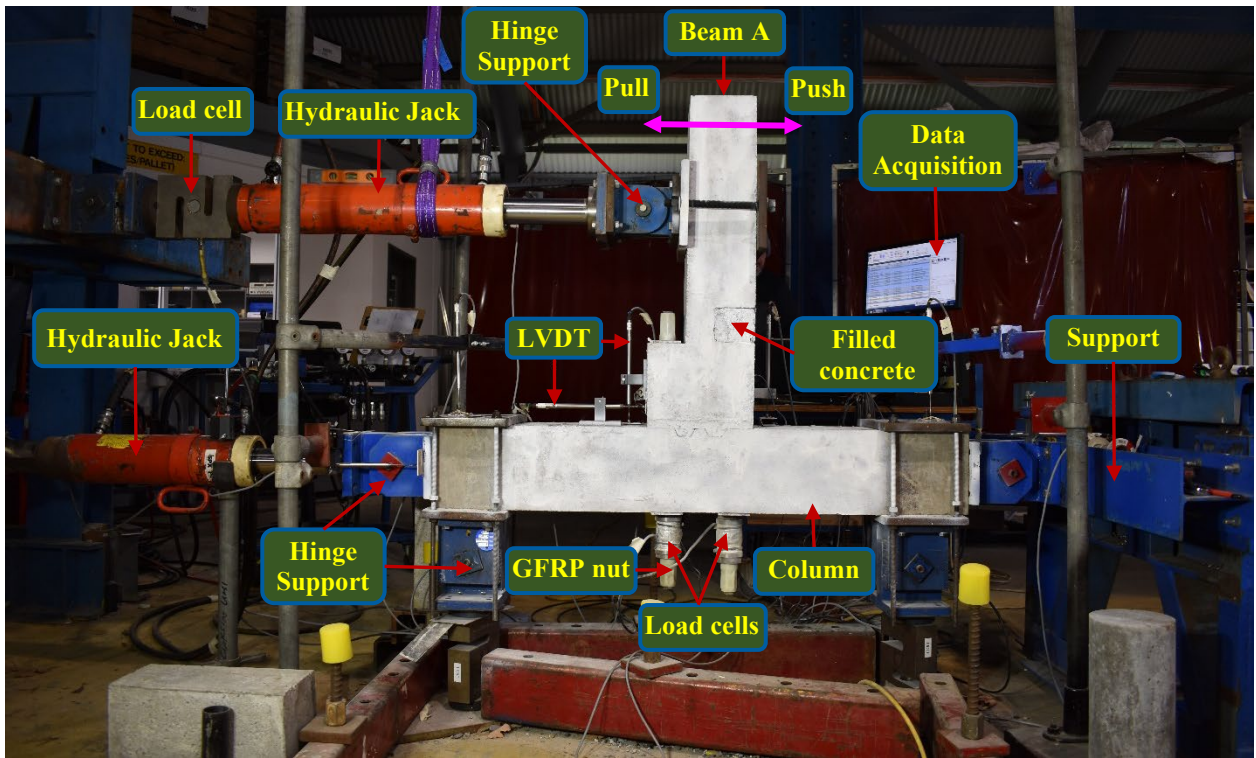
201   **Fig 5.** Typical test setup of hybrid joints.
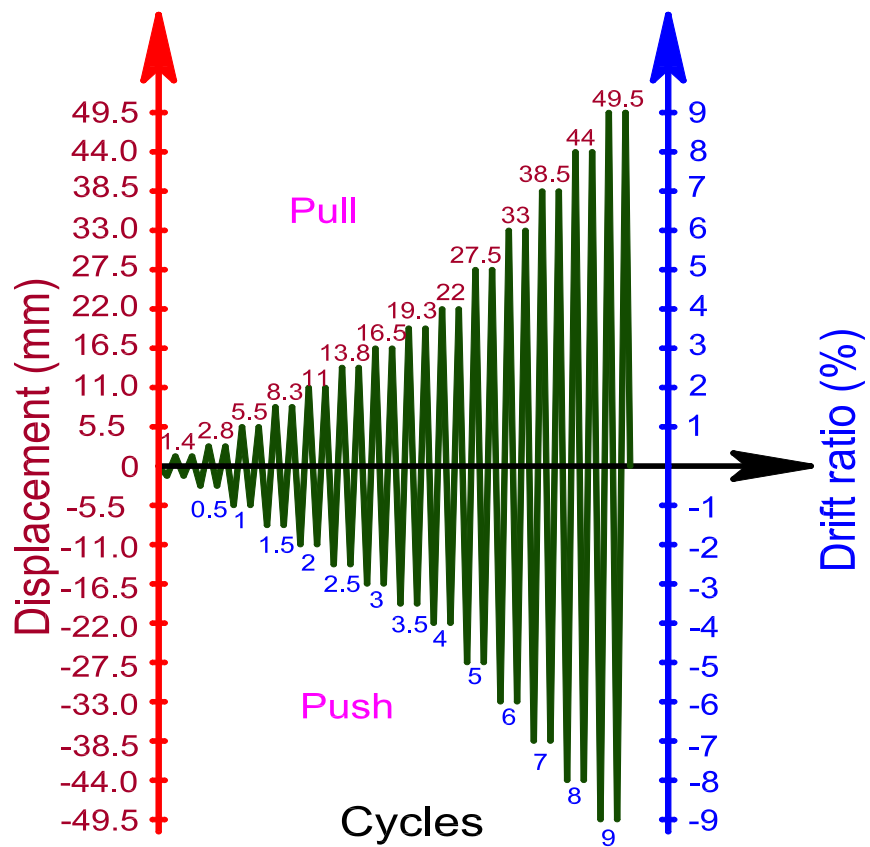
202

203 **Fig 6.** Loading history.

2.3 Material properties

205 Ready-mixed concrete from Boral Pty Ltd [32] was used to cast all the specimens in this study (see

206 the mixture in Table 2). The concrete properties were determined according to AS 1012.8.1-14 [33]

207 and AS 1012.9.1-14 [34] standards. , the 28th-day compressive strength (f'_c) and tensile strength (f_{ct})

208 of group 1 (M1-SR, D5-SR-S-T200 and D6-GR-S-T100) were 38.5 MPa and 3.8 MPa, respectively

209 whereas the 65th-day of group 2 (M2-GR, H3-GR-T200, and H4-GR-T100) were 59.1 MPa and 4.2

210 MPa, respectively. The mechanical properties of the two groups were different due to different

211 concrete batches and testing days. This difference was also reported in some previous studies [1, 2,

212 35-37]. The mixture of the high strength concrete with the compressive strength of 75.2 MPa used to

213 fill the gap in hybrid joints as shown in Fig. 3 is presented in Table 2. GFRP bolts and nuts were

214 supplied by Bluey Pty Ltd [38]. The nominal tensile force of threaded rods (350 kN) was significantly

215 higher than the failure force of the nuts (70 kN). Therefore, the capacity of the whole bolts was

216 governed by the capacity of nuts. The mechanical properties of GFRP bolts are presented in Table 3.

217 The mechanical properties of GFRP reinforcements, which were sponsored by Pultrall Inc [39], are

218 summarized in Table 4. The mechanical properties of GFRP bolts and reinforcements were provided

219 by the suppliers. Steel reinforcement properties are presented in Table 5.

220 **Table 2.** Mixture proportions of 1 m³ plain concrete [32] and filled concrete.

Materials	Unit	Ready-mixed concrete	Filled concrete
Sand	(kg/m³)	534	1051
7-mm coarse aggregate	(kg/m³)	1100	-
Coarse sand Gin Gin	(kg/m³)	225	-
Cement	(kg/m³)	400	995
Water	(L/m³)	175	180
Plastiment BV35	(L/m³)	1.6	-
Viscocrete 10	(L/m³)	1.2	-

Materials	Unit	Ready-mixed concrete	Filled concrete
Viscoflow 15	(L/m^3)	1.2	-
Silica fume	(kg/m^3)	-	238
Superplasticizer	(kg/m^3)	-	67
Steel fibre (35 mm)	(%)	-	2

Note: - = not applicable.
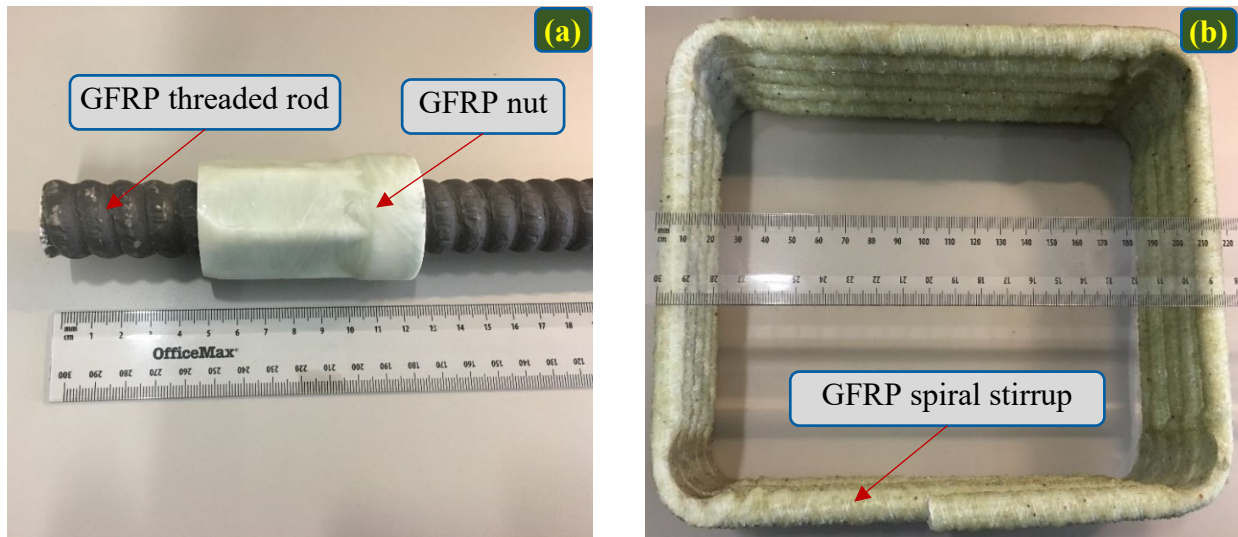
Fig. 7. Details of (a) GFRP bolts and (b) GFRP spiral stirrups.

Table 3. Properties of GFRP bolts and nuts [38].

Names	Nominal diameter	Nominal cross-section area	Shear @90°	Shear @50°	Ultimate load	Elastic modulus	Weight
	(mm)	(mm^2)	(kN)	(kN)	(kN)	(GPa)	(kg/m)
Bolt	25	346	170	345	≥ 350	60	0.9
Nut	25	-	-	-	70	60	-

Note: - = not applicable.

Table 4. Mechanical properties of GFRP reinforcements [39].

| Nominal diameter	F_u	f_u	F'_u	f'_u	Q_{sh}	F_{sh}	E_s	Area	Notes
(mm)	(kN)	(MPa)	(kN)	(MPa)	(kN)	(MPa)	(GPa)	(mm^2)	
10.5	89.7	1259.2	42.3	593	33.6	235.8	54	87	Stirrups
17.1	268.9	1358.3	132.4	668.8	82.5	208.5	54	230	Longitudinal reinforcements

Note: F_u and f_u = Load at the break and tensile strength of the straight portion.
F'_u and f'_u = Load at the break and tensile strength of the bent portion.
Q_{sh} and f_{sh} = Load at the break and transverse shear strength.
E_s = Elastic modulus.

Table 5. Steel reinforcement properties.

Bar size (mm)	Area (mm²)	f_y (MPa)	f_u (MPa)	E_s (GPa)	Remarks
10	78	560	675	200	Stirrups
16	201	597	706	200	Longitudinal reinforcements

3. Experimental results and discussion

3.1 Global performances and failure modes

In the beam-column joints, there were three possible failure positions including the joint area, fixed-end of the beam, and a combination of the joint area and fixed-end. Either shear failure or compressive strut failure mainly governed the failure patterns in the joint area while flexural cracks and concrete crushing dominated failure modes at the fixed-end [2]. Fig 8 shows the failure modes of all the specimens tested in this study. To consider the effects of the shear keys on the joint performances, a comparison was conducted between specimens with shear keys and without shear keys. The shear keys were utilized at the interface between the columns and CEPs of the precast joints (excepting Specimen D5-SR-S-T200) to resist the shear forces. Therefore, no-slip between the column and CEP was observed during the tests. Meanwhile, despite no shear keys on Specimen D5-SR-S-T200, no-slip was recorded on this specimen either because the friction between the column and CEP surfaces was sufficient to resist the shear force. Although the maximum tensile forces in GFRP bolts almost reached their nominal capacity of the GFRP nuts (see Table 3), no failure was observed on GFRP nuts. For instance, the maximum tensile force of GFRP bolts of Specimen H3-GR-T200 was 69 kN which almost reached the nominal capacity of the GFRP nuts (70 kN). After testing, all GFRP nuts were carefully checked and showed good conditions without damage. Fig. 9 shows strain of longitudinal reinforcements and middle stirrups in the CEP. The strain of steel and GFRP

252 reinforcements at the peak load was lower than the yield strain (2,985 $\mu\varepsilon$) and the nominal strain at

253 the break strength (25,238 $\mu\varepsilon$), respectively. For instance, strain of the longitudinal reinforcements of

254 Specimens M1-SR, M2-GR and D6-GR-S-T100 was 2,233 $\mu\varepsilon$, 9,666 $\mu\varepsilon$, and 3,994 $\mu\varepsilon$, respectively.

255 The above results proved that steel and GFRP reinforcements did not govern the main failure of the

256 specimens so concrete dominated the main failure of the specimens. These results indicate that the

257 structures using GFRP materials satisfy the design requirements for not suffering brittle failure. On

258 the other hand, strain of the longitudinal reinforcements of Specimen M2-GR was around four times

259 higher than that of Specimen M1-SR at the peak load. Lower elastic modulus of GFRP reinforcements

260 (54 GPa), compared to that of steel reinforcement (200 GPa) caused the above difference. The lower

261 modulus of GFRP also led to a higher DR of the specimens using GFRP reinforcements. More

262 discussions about DR will be given in the subsequent section.
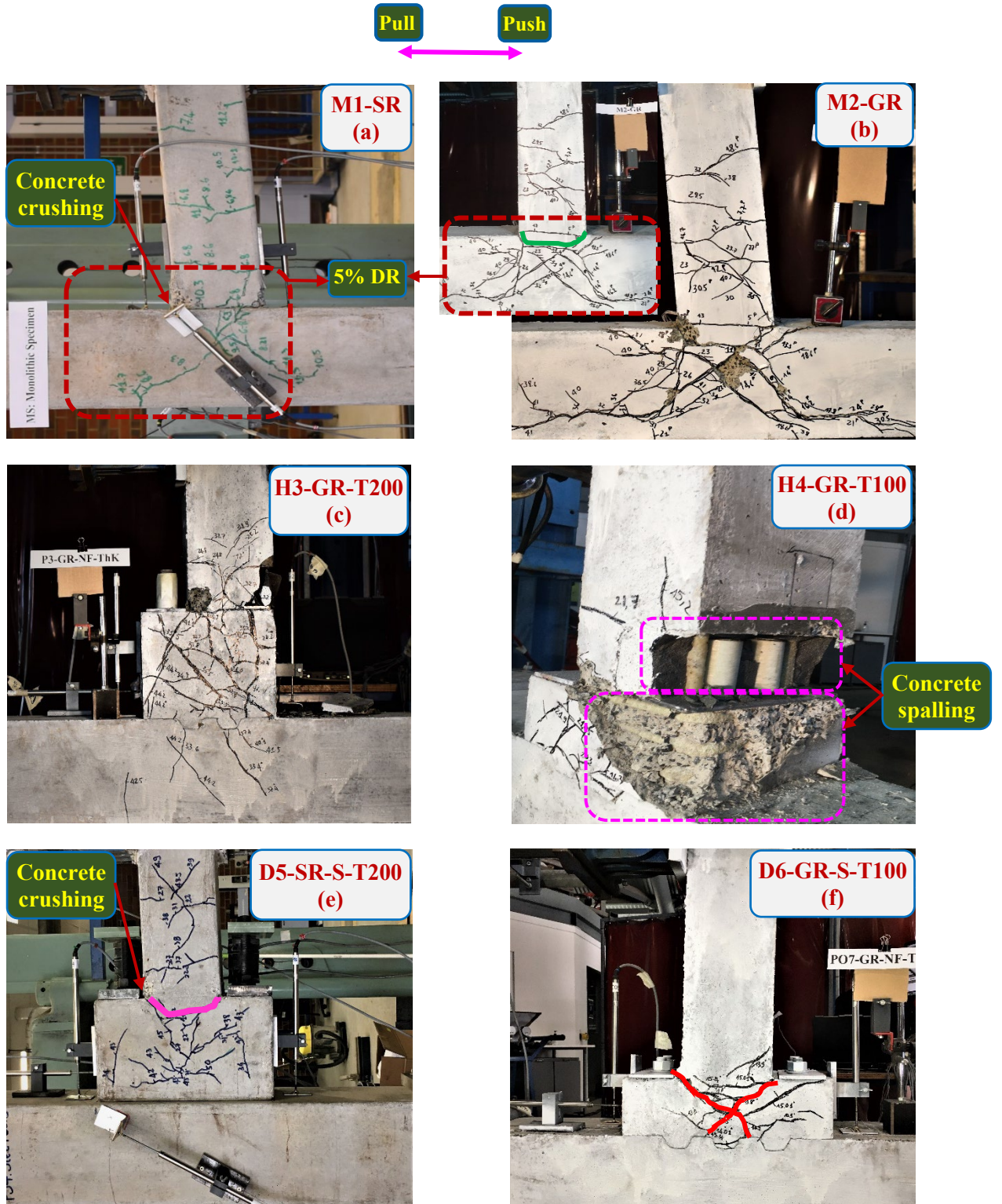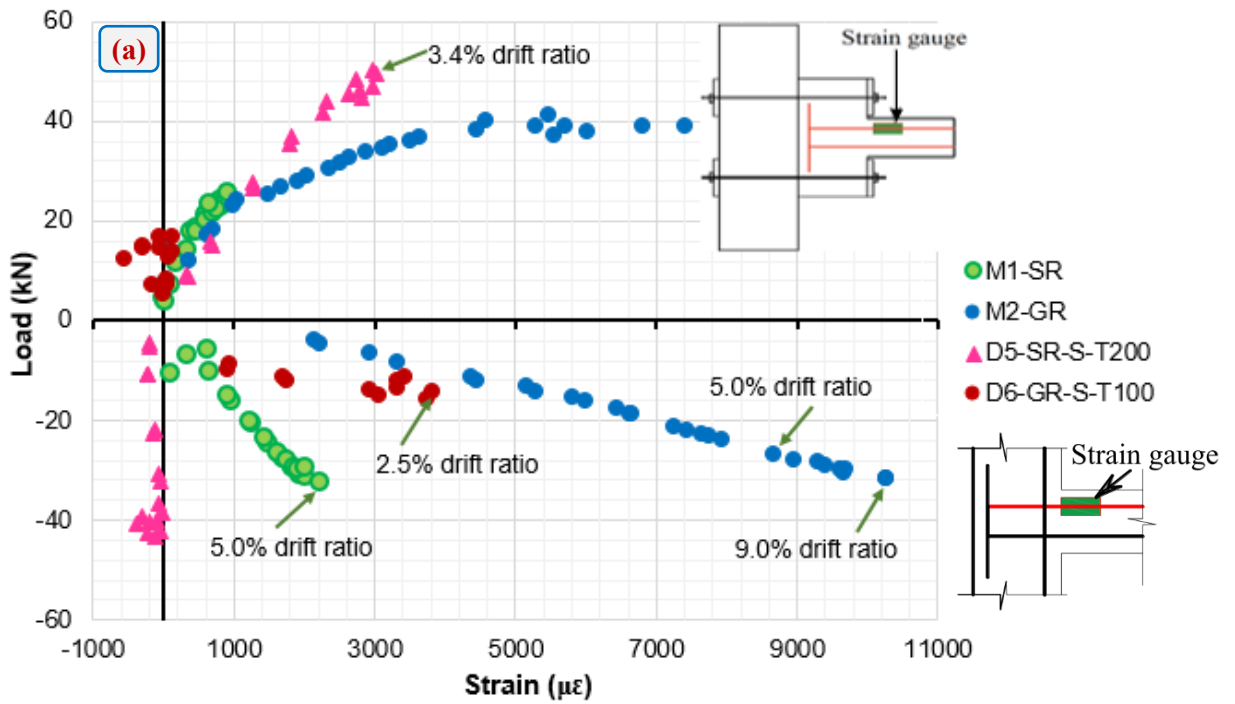
Fig. 8. Failure modes.

To evaluate if the specimens failed in the beam or the joint area, it is necessary to estimate the capacity of the beam, together with the observation during the test. This study adopted ACI 318-11 [40] to estimate the loading capacity of the beams with steel reinforcements and ACI 440.1R-15 [41] for that

267 of beams with GFRP reinforcements. The calculations showed that the design capacities of the beams

268 of Specimens M1-SR, M2-GR, D5-SR-S-T200, and D6-GR-S-T100 were 28.1, 32.9, 44.2, and 33.2

269 kN, respectively. The loading capacity of the beam of Specimen M2-GR was higher than that of

270 Specimen M1-SR due to higher concrete compressive strength and larger beam width. The concrete

271 compressive strength and beam width of Specimen M2-GR were 59.1 MPa and 200 mm, respectively,

272 whereas those of M1-SR were 38.5 MPa and 150 mm, respectively. The loading capacity of the beams

273 of Specimens H3-GR-T200 and H4-GR-T100 was 50.1 kN and 39.7 kN, respectively. It is noted that

274 the actual applied loads on the beam of the hybrid joints were lower than the respective loading

275 capacity due to the spalling failure of the filled concrete block due to poor bonding between the filled

276 higher strength concrete and the normal concrete of the beam. In addition, the loading capacity of the

277 joint was defined at the corresponding loading value when failure occurred in the joint area. There

278 have been no standards to estimate the joint capacity of the hybrid and dry joints. Therefore, based

279 on the above-estimated loading capacity of the beams, if the applied peak loads to the specimens were

280 lower than the loading capacity of the beams, the failure of these specimens was governed by other

281 parts, i.e. joint area. Otherwise, these specimens might fail in the beam of the specimens with the

282 monolithic or dry joints or a combined failure in both the beam and joint of the specimens with the

283 hybrid joint. From the observation during the tests and the comparisons between the design loading

284 capacities and the applied peak loads in the tests, it could be concluded that Specimens M1-SR and

285 D5-SR-S-T200 failed in the beam at the fixed-end while the primary failure of Specimen D6-GR-S-

286 T100 occurred in the joint area. The combined beam and joint failure was observed on Specimens

287 M2-GR because both the beam and joint areas reached their ultimate strength. For Specimens H3-

288 GR-T200, and H4-GR-T100, the combined failure at the joint and beam areas was also observed. The

289 reason for these failure positions can be explained that the joint area reached its ultimate strength after

290 the low bonding between old and new concrete at the filled concrete caused the failure of this section

291 of the beam.

292
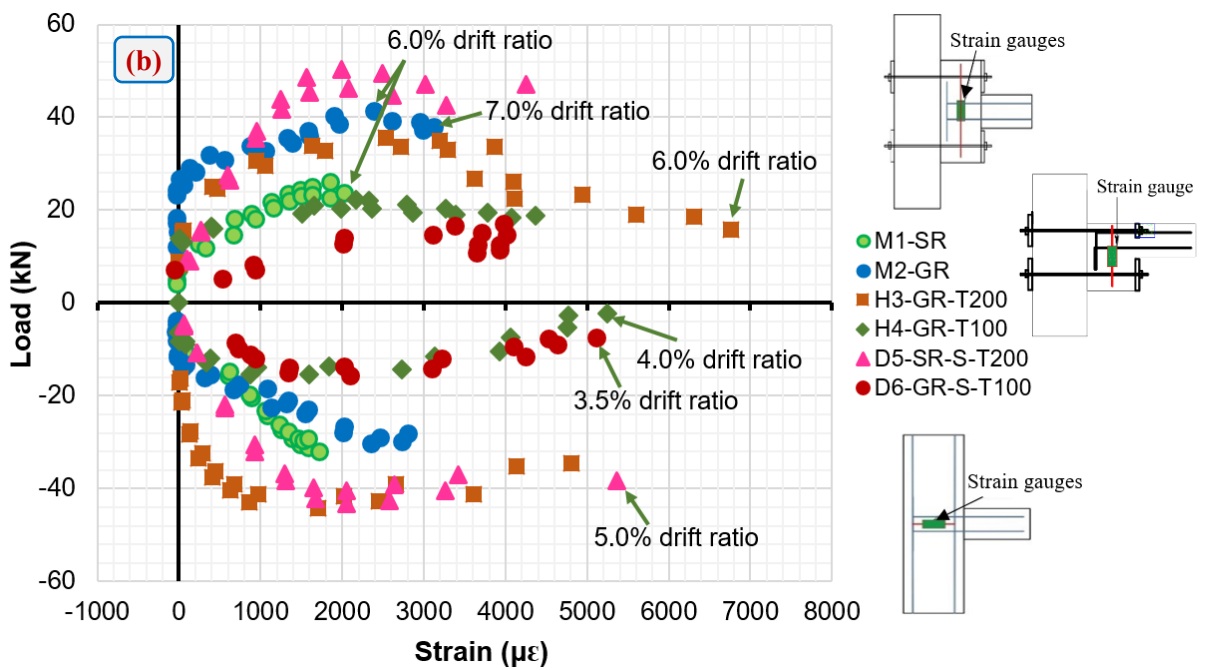
293

294   **Fig. 9.** Data of strain gauges attached on (a) longitudinal reinforcements and (b) stirrups at middle
295   joints.

296   To evaluate the failure modes of the specimens using steel and GFRP reinforcements, a comparison

297   was conducted between Specimens M1-SR and M2-GR. In general, the failure modes of these

298   specimens were similar at the same DR. Flexural cracks occurred quite early at the fixed-end of the

299 beam when the beam soffit was in tension at 0.3-0.5% DR. Afterwards, the flexural cracks extended

300 to the loading point at 100 and 200 mm from the fixed-end. After 1% DR the inclined cracks tended

301 to propagate to the joint area. However, there were three different types of failure modes in these two

302 specimens. (1) Although the trend of the inclined cracks in the joint area was similar, more inclined

303 cracks were observed in the joint area of Specimen M2-GR, compared to Specimens M1-SR. It is

304 attributed to the displacement applied during the tests. The beam width of Specimens M2-GR (200

305 mm) was larger than that of Specimen M1-SR (100 mm). As a result, it required a larger force to

306 deform the beam of Specimen M2-GR than that of Specimen M1-SR and, therefore, caused more

307 cracks in the joint area of Specimens M2-GR at the same drift ratio of Specimen M1-SR, as shown

308 in Fig. 8(a) and 8(b) at 5% DR. (2) Crushing of concrete was observed in Specimen M1-SR at 2%

309 DR whereas no crushing of concrete appeared on Specimen M2-GR until 5% DR. This different

310 performance was attributed to the different concrete compressive strength of these specimens. Higher

311 concrete compressive strength of Specimen M2-GR (59.1 MPa) well resisted the compressive stress

312 in concrete, compared to Specimen M1-SR (38.5 MPa). (3) Especially, more severe damage was

313 observed on Specimen M2-GR after the test, compared to Specimen M1-SR. It is because the elastic

314 modulus of GFRP reinforcements (54 GPa) was lower than that of steel reinforcements (200 GPa).

315 The lower elastic modulus caused higher elongation of GFRP reinforcements, compared to steel

316 reinforcements. For instance, at the same 5% DR, strain of the longitudinal GFRP reinforcements

317 (8,685 με) was 3.9 times higher than that of the longitudinal steel reinforcements (2,233 με), see Fig.

318 9(a). At the end of the tests, Specimen M2-GR showed larger displacement (10.5% DR), compared

319 to Specimen M1-SR (6.5% DR). Larger displacement caused more severe damage in the joint area

320 and concrete crushing at the fixed-end of Specimen M2-GR.

321 Figs. 8(c) and 8(d) illustrate the main failure modes of the two-hybrid joints (H3-GR-T200 and H4-

322 GR-T100) with different thicknesses of the CEP (200 vs 100 mm). In general, the failure positions of

323 these two specimens were similar that both the specimens failed at the fixed-end and in the joint area.

324   Although the beams of these two specimens did not reach their loading capacity (50 kN for Specimens

325   H3-GR-T200 and 39.7 kN for H4-GR-T100), severe damage and concrete spalling were observed at

326   the fixed-end and in the joint area of these two specimens, as shown in Figs. 8(c) and 8(d). It is

327   attributed to the low bonding strength between old and new concrete surfaces. This low bonding

328   caused initial cracks around the filled concrete block at a low DR of 0.5-1% in the pull direction and

329   led to damage of the filled concrete block in the push direction. Consequently, the cross-section of

330   the beam reduced and caused more severe damage at the fixed-end. At the first cycle of 1% DR, the

331   inclined cracks started at the fixed-end and propagated to the middle zone of the CEP. Tensile and

332   shear cracks governed the main failure of these two specimens. Therefore, strain of middle stirrups

333   in the joint area was relatively high. For example, the strain of Specimen H3-GR-T200 at the peak

334   load (2.5% and 3.5% DR) was 2,723 and 3,866 $\mu\varepsilon$, respectively (see Fig. 9(b)). It is noted that the

335   inclined cracks were only observed on the column of Specimen H3-GR-T200 from 1.5% DR while

336   no cracks appeared on the column of Specimen H4-GR-T100 and other precast joints. The application

337   of the shear key helped to transfer the shear force into the column and induced inclined cracks in the

338   column of Specimen H3-GR-T200. As a result, the inclined cracks were generated on the column of

339   Specimen H3-GR-T200 only. For Specimens H4-GR-T100 and D6-GR-S-T100, although shear keys

340   were also applied on these specimens, no inclined cracks were observed on the column due to weak

341   shear resistance at CEP with a thin thickness of 100 mm. Therefore, for Specimens H4-GR-T100 and

342   D6-GR-S-T100, the CEP reached their ultimate shear capacity before the column. Lower shear

343   resistance of the CEP of Specimen H4-GR-T100, compared to Specimen H3-GR-T200 also caused

344   more severe damage to the CEP of Specimen H4-GR-T100, as shown in Figs. 8(c) and 8(d). In

345   general, the failure of Specimens H3-GR-T200 and H4-GR-T100 was governed by the CEP.

346   Figs. 8(e) and 8(f) show a comparison of failure modes between two dry joints with different

347   thicknesses of the CEP (100 vs 200 mm). In general, the failure modes of the two specimens were

348   different. Specimen D5-SR-S-T200 failed at the fixed end of the beam whereas Specimen D6-GR-S-

349   T100 failed in the joint area. The flexural cracks (see the pink curve in Fig. 8(e)) and crushing of

350   concrete at the fixed-end mainly governed the main failure modes of Specimen D5-SR-S-T200 due

351   to the greater shear resistance of the CEP. Therefore, in the dry joint with the CEP thickness of 200

352   mm, the ultimate bending capacity of the beam was reached before the shear capacity of CEP. For

353   Specimen D6-GR-S-T100, due to a reduction of the CEP thickness from 200 mm to 100 mm, the

354   shear resistance of the CEP of Specimen D6-GR-S-T100 was significantly reduced. Consequently,

355   various inclined cracks were generated in the middle zone of the CEP (see the red curves in Fig. 8(f)).

356   The inclined cracks of these two dry joints only concentrated in the middle zone of the CEP due to

357   higher shear stress concentrated in the middle zone, compared to the right and left zone of the CEP.

358   High prestress force in the bolts increased the confined capacity of concrete in the right and left zone

359   of CEP [1, 3]. Therefore, fewer cracks were observed in these zones. This finding will be validated

360   in the next section using numerical simulation with ABAQUS. Finally, almost no cracks on the beam

361   of Specimen D6-GR-S-T100 while some flexural cracks appeared on Beam A from the fixed-end to

362   the loading point of Specimens D5-SR-S-T200. It is because Specimen D6-GR-S-T100 failed very

363   early before Beam A reached its ultimate bending capacity. The above results indicated that reducing

364   the CEP thickness changed the failure mode from the beam to the joint area.
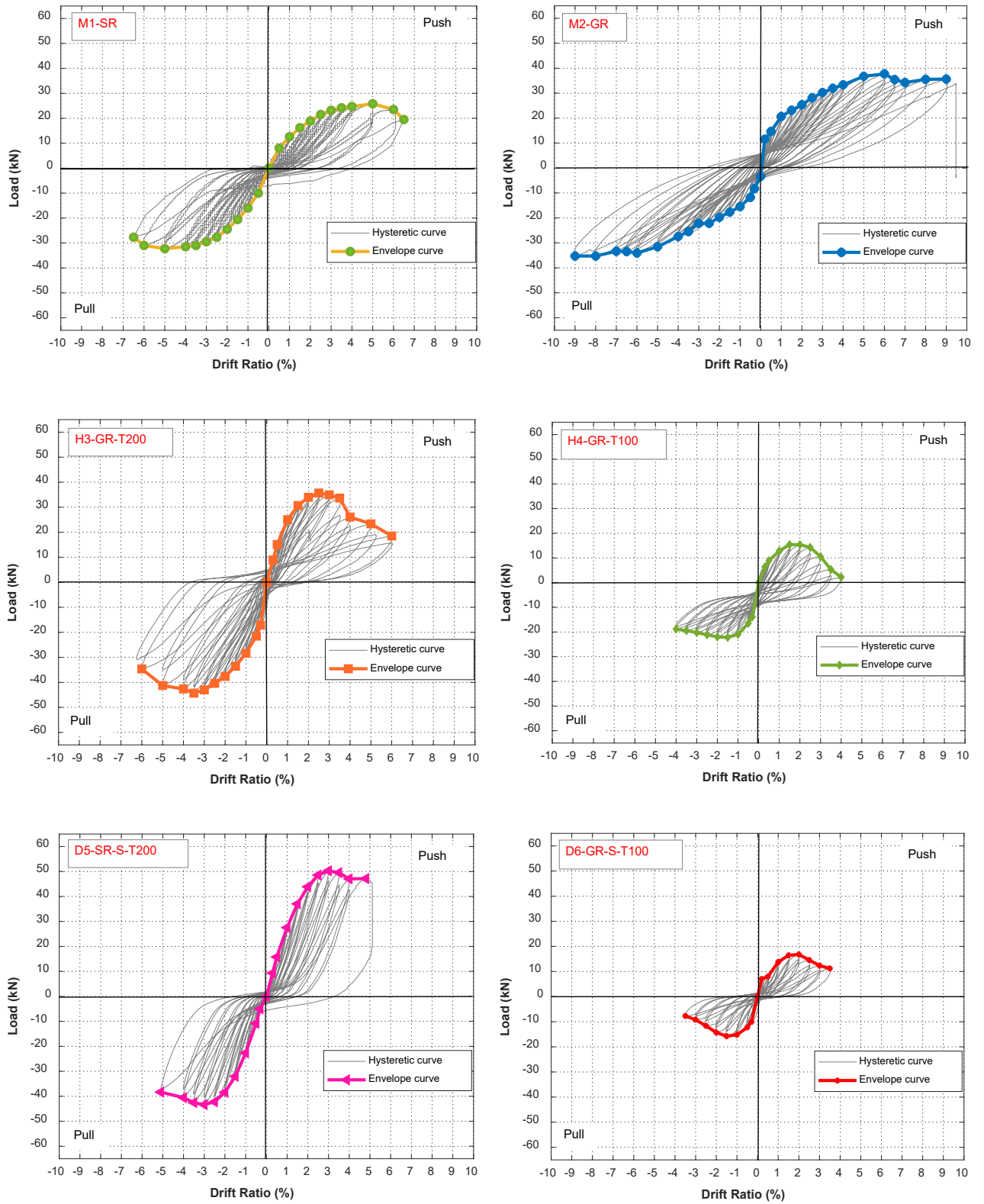
365   **3.2 Hysteretic responses**

366   Both the hysteretic and envelope curves of the monolithic and dry joints were approximately

367   symmetrical in the push and pull directions (see Figs. 10 and 11) due to the identical longitudinal

368   reinforcements. However, those of the hybrid joints (H3-GR-T200 and H4-GR-T100) were

369   asymmetrical in these directions owing to the asymmetric designs of the CEP (see Figs. 1 and 2). The

370   hybrid joints showed ductile performance in the pull direction while the applied load quickly reduced

371   in the push direction after reaching the peak load. For instance, at 4% DR, Specimen H4-GR-T100

372   retained 85% of the post-peak load in the pull direction while it completely failed (almost zero applied

373   load) in the push direction. This phenomenon is attributed to (1) the gaps on the beams owing to the

374   spalling failure of concrete filling the slot of the hybrid joints as discussed above, and (2) the effect

375   of the CEP thickness. The longitudinal reinforcements well resisted the tensile stress in the beam in

376   the pull direction. Meanwhile, the filled concrete block was damaged in the push direction due to the

377   low bonding between old and new concrete surfaces. In addition, reducing the CEP thickness caused

378   severe damage in the joint area which mainly affected the loading capacity in the push direction, as

379   shown in Fig. 8(d). The above two reasons led to significantly different loading capacity in the two

380   directions. Fortunately, the hybrid joints indicated greater performances in the pull direction (primary

381   loading direction in the real joint application), compared to the push direction. Therefore, this newly

382   proposed hybrid joint could be effectively applied to structures in seismic-prone areas to reduce

383   construction cost. For high seismic-prone areas, the bonding between old and new concrete surfaces

384   needs to be improved and further studies are deemed necessary.

385   The hysteretic curves of Specimens M1-SR and M2-GR in Fig. 10 indicate typical different

386   behaviours of the specimens using the steel and GFRP reinforcements. Due to linear behaviours up

387   to rupture of the GFRP reinforcements, smaller residual displacement (2.8 mm) was recorded in

388   Specimen M2-GR, compared to Specimen M1 (13.8 mm) at the same 5% DR. The beams of the

389   specimens using GFRP reinforcements could return back to its original position after unloading. It

390   means the application of GFRP reinforcements did not induce brittle failure of the tested beam-

391   column joints in the testing range in this study while the great centring capability was observed on

392   specimens using GFRP reinforcements. This observation was also reported in another study with the

393   dry joints using GFRP bolts and reinforcements under impact loading [30]. The yielding of steel

394   reinforcements induced larger residual displacements for Specimen M1-SR. It is noted that concrete

395   should govern the main failure modes in all specimens using GFRP reinforcements to avoid brittle

396   failures. This principle should be applied in designs of the beam-column joints using GFRP materials.

Fig. 10. Hysteretic responses of all the specimens.

Load-drift ratio envelopes
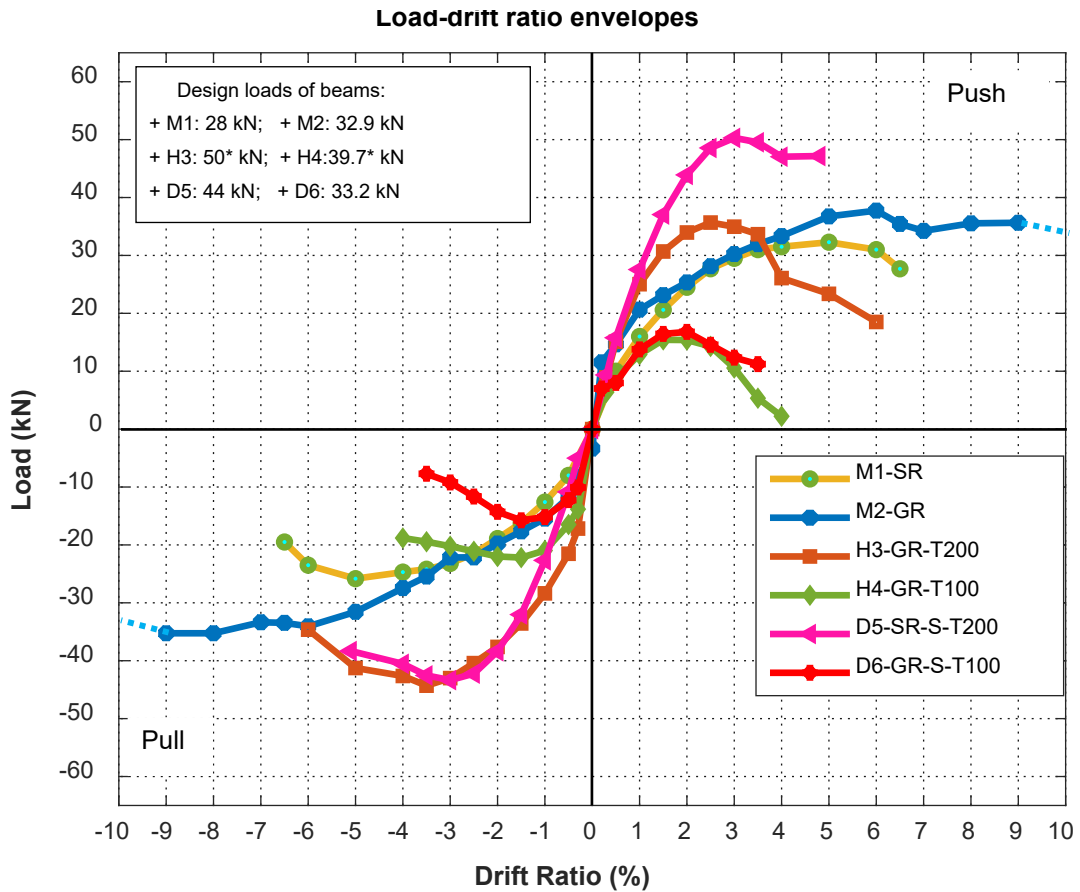
Fig. 11. Envelope curves of the tested specimens.

Note: * = estimated value based on the beam without gap.

3.3 Energy dissipation capacity

Energy dissipation (ED) is an important parameter to evaluate the performance of a structure under earthquake loading. The beam-column joints are considered to have good performances under seismic loading if they can dissipate sufficient energy while retaining their stiffness and loading capacity. The ED of the beam-column joint under cyclic loading is determined based on the area enclosed inside the hysteretic loop in the first of every two cycles. As depicted in Fig. 12, the ED of all the specimens was analogous up to 1% DR owing to the elastic performance in the initial stage. After that the ED of the specimens was different. In general, the ED of the dry and hybrid joints (H3-GR-T200 and D5-SR-S-T200) was greater than that of the corresponding monolithic joints (M1-SR, M2-GR). For instance, the ED of the precast joints (hybrid and dry joints) was approximately 57-74% higher than

27

412   that of the monolithic joints at 4% DR. It means the proposed dry and hybrid joints showed excellent

413   ED under seismic loading and therefore are superior for applications in structures in seismic-prone

414   areas. There are two possible reasons to explain this promising result. (1) Under cyclic loading, the

415   joint opening was observed in the precast joints at the excessive load and the joint closed after

416   unloading due to the prestress forces and linear performance of the bolts. This behaviour led to better

417   ED in the precast joints due to friction between interfaces and damping of material, as compared to

418   the monolithic joints in which ED depends mainly on plastic deformation and damage of structural

419   materials. (2) Given the same drift ratio, precast joints have higher loading capacity in each cycle,

420   compared to the monolithic joints, which led to greater ED. Therefore, the above results suggest that

421   the precast joints could well replace the monolithic joints in seismic-prone areas.

422   To further evaluate whether the application of GFRP reinforcements affected the ED of beam-column

423   joints, a comparison was conducted between Specimen M1-SR using steel reinforcements and

424   Specimen M2-GR using GFRP reinforcements (see Fig. 12). In general, the ED of the both specimens

425   was analogous while marginal higher ED was observed in Specimen M2-GR, as compared to

426   Specimen M1-SR from 1.5% DR to 4.5% DR. This positive result is attributed to fat hysteretic loops

427   and higher applied load in Specimen M2-GR using GFRP reinforcements. Although GFRP

428   reinforcements showed linear performances up to rupture, fat hysteretic loops were observed on

429   Specimen M2-GR because GFRP reinforcements have lower stiffness compared to the steel

430   reinforcements, therefore likely led to more concrete damage although the concrete strength of M2-

431   GR was higher than that of M1-SR. In addition, GFRP reinforcements in this study were designed to

432   avoid rupture failure during the test and concrete governed the main failure modes of the specimens,

433   as illustrated in Section 3.1. The applied load of Specimen M2-GR was higher than that of Specimen

434   M1-SR due to the linear behaviour and higher strength of GFRP reinforcements than steel

435   reinforcements, as well as the higher concrete compressive strength and larger beam width. The

436   loading capacity of M1-SR would not substantially increase after the steel yield. Nonetheless, the

current comparison may not be valid if the concrete strength and beam size of M1-SR and M2-GR were the same, i.e., steel reinforcement might lead to more ED because of steel yielding. Nonetheless, these results indicate that the application of GFRP reinforcements can meet the ED requirements of beam-column joints under seismic loading.
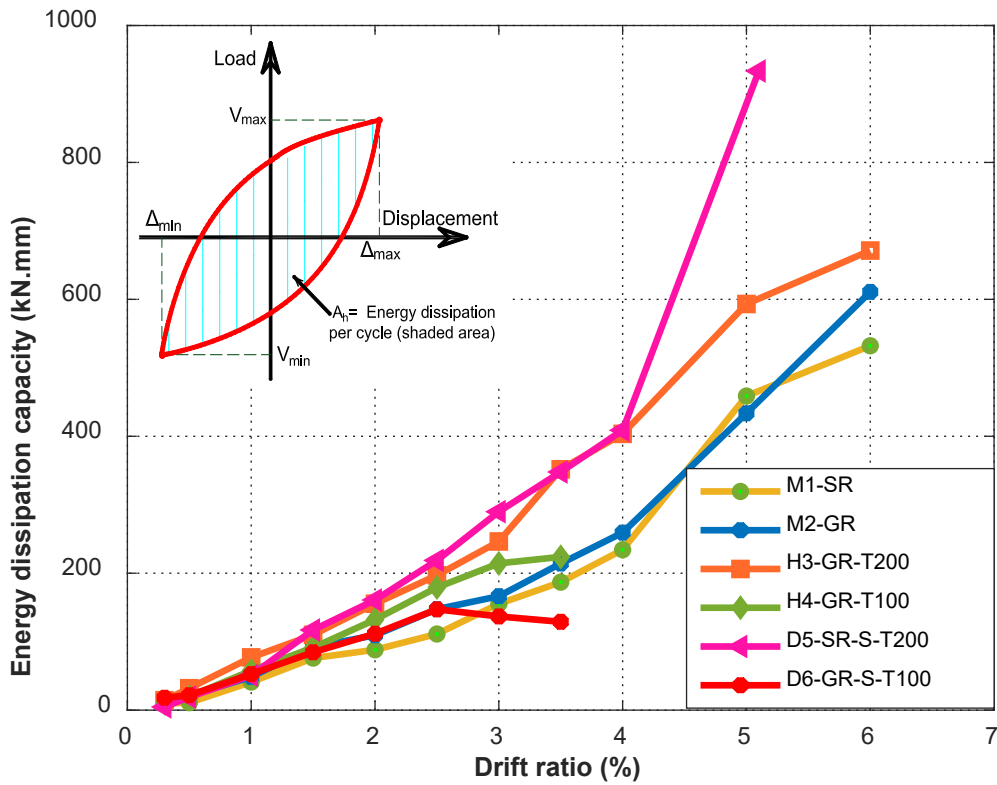
Fig. 12. Energy dissipation of all the specimens.

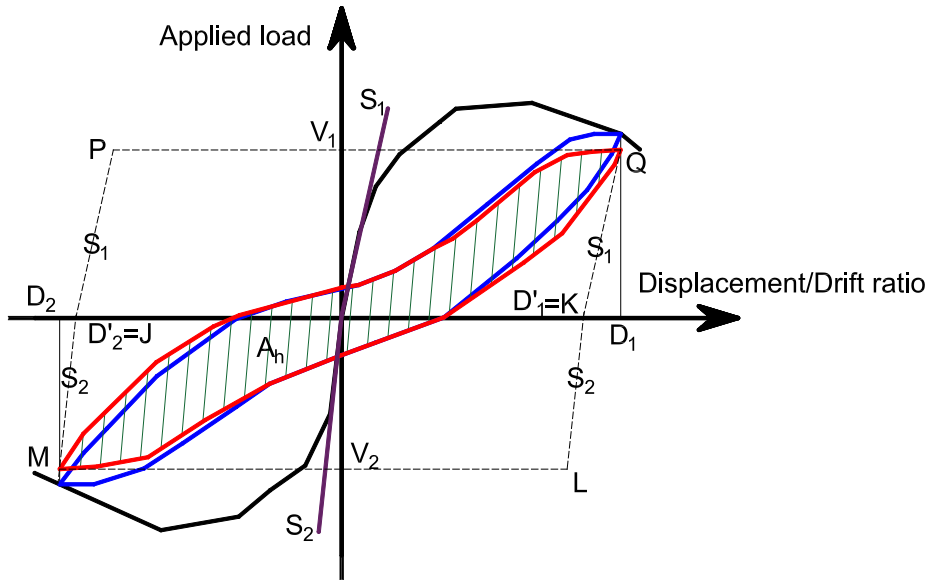**Table 6.** Relative energy dissipation ratio of all the specimens based on ACI 374.1-05 [42].

Specimens	Drift ratio	A_h (kN.%)	V_1 (kN)	V_2 (kN)	D'_1 (%)	D'_2 (%)	E_r
M1-SR		27.02	22.85	29.44	2.20	1.90	0.126
M2-GR		35.05	34.20	21.40	2.55	2.10	0.136
H3-GR-T200	3.50%	61.79	26.76	41.67	2.70	2.50	0.174
H4-GR-T100		30.86	2.75	18.32	3.30	3.00	0.232
D5-SR-S-T200		50.73	44.70	39.10	2.10	1.75	0.157
D6-GR-S-T100		23.46	11.23	7.71	3.10	3.25	0.195

445 To evaluate the energy dissipation capacity of beam-column joints under seismic loads, ACI 374.1-
446 05 [42] provides acceptance criteria at the last loading cycle of 3.5% drift ratio. Based on ACI 374.1-
447 05 [42], the relative energy dissipation ratio (E_r) is defined as the ratio of the area (A_h) inside the
448 applied load-drift ratio/displacement loop to the area of the effective circumscribing parallelograms
449 *JPQK* and *KLMJ* (see Fig. 13). The areas of the parallelograms are equal to the sum of the absolute
450 values of the applied loads (V_1 and V_2), at the drift ratios (D_1 and D_2) multiplied by the sum of the
451 absolute values for the drifts ratios (D'_1 and D'_2), as presented in Eq. (1) [42]:

$$E_r = \frac{A_h}{(V_1+V_2)(D'_1+D'_2)} \qquad (1)$$

453 Table 6 gives the results of the relative energy dissipation ratio. Given that the relative energy
454 dissipation ratios (E_r) of all the specimens are greater than 1/8 (0.125), all the specimens satisfy the
455 requirements of ACI 374.1-05 [42] in maintaining the stablity of a structure before it collapses.

Fig. 13. Main parameters to determine relative energy dissipation ratio.

3.4 Drift ratio and maximum applied loads

459 Drift ratio is a crucial parameter to evaluate the ductility of structures under earthquake loading. This
460 parameter is determined based on the ratio of beam displacement at the loading point (Δ) and the
461 beam length from the column surface to the loading point (l=550 mm), as denoted below:

$$R = \Delta/l \qquad (2)$$
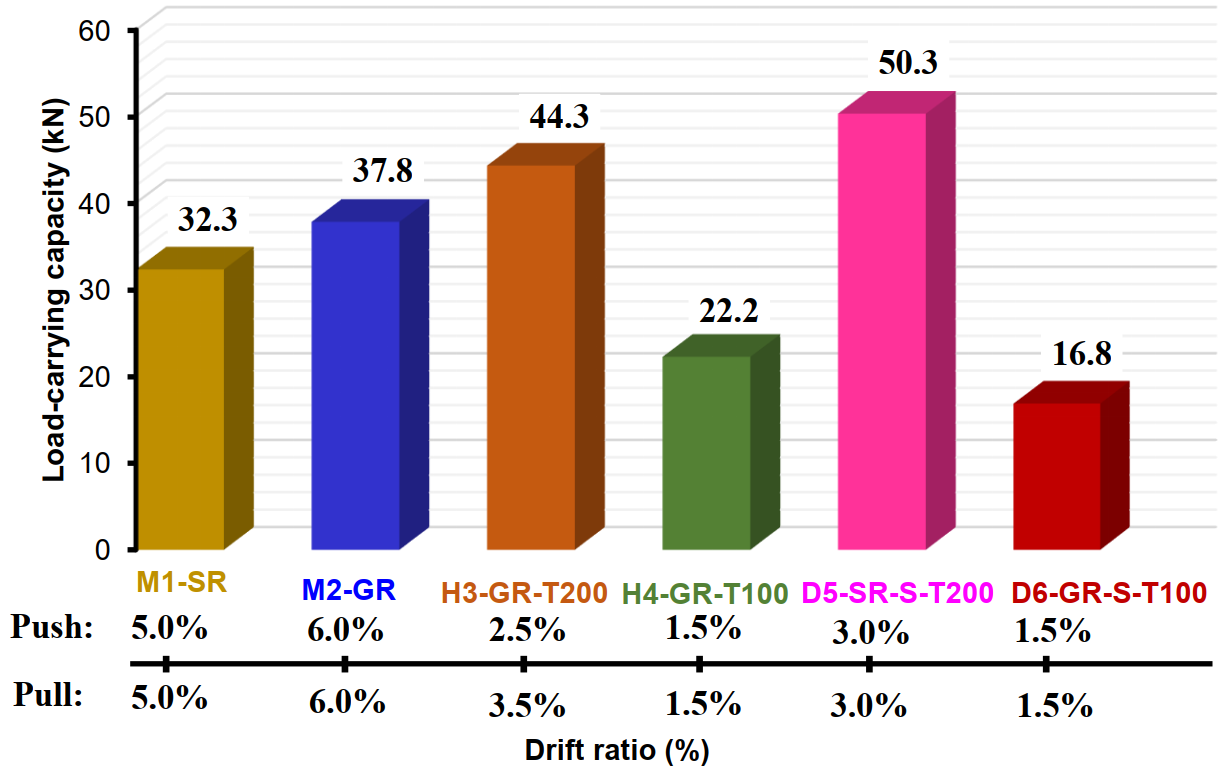
Fig. 14. Comparison of peak load and drift ratio.

A comparison of the peak loads and the corresponding DRs is presented in Fig 14. In general, the application of GFRP reinforcements illustrated good performances in terms of the peak load and DR, compared to the corresponding steel reinforcements. Specimen M2-GR reached 6% DR which was higher than that of Specimen M1-SR (5% DR). This DR well exceeds the requirements for the immediate occupancy structural performance level (2% DR) and the life safety structural performance level (3% DR) in ASCE 41-17 [10]. This result could be explained that this study as well as many studies [36, 43-50] adopted the high-performance levels of structures as a criterion in evaluating the performance of the studied structural joints. For example, the criterion corresponding to the collapse prevention (5% DR) was adopted in this study. The results demonstrated that the joints in this study did not completely lose its load-carrying capacity at 5% DR, indicating they would satisfy the collapse prevention requirement. In addition, lower elastic modulus and higher rupture strength of GFRP reinforcements resulted in better DR of Specimen M2-GR, compared to Specimen M1-SR using steel reinforcements. In addition, although GFRP reinforcements had lower elastic modulus as compared

478 to steel reinforcements, the higher peak load was recorded on Specimen M2-GR. There are three

479 reasons to explain this result. (1) The concrete compressive strength of Specimen M2-GR (59.1 MPa)

480 was higher than that of Specimen M1-SR (38.5 MPa). (2) The beam width of Specimen M2-GR was

481 200 mm, while that of M1-SR was 150 mm. (3) GFRP reinforcements did not rupture in the tests due

482 to its high strength. Therefore, their resistance increases linearly with the DR and applied load,

483 whereas the loading resistance from steel reinforcements would not increase once they yield. In

484 general, the results above demonstrate that the application of GFRP reinforcements did not cause

485 brittle failure, thus they could be potentially applied in seismic-prone regions.

486 The hybrid joint shows sufficient loading capacity and DR, compared to the monolithic and dry joints.

487 As shown in Fig. 14, the peak load of Specimen H3-GR-T200 (44.3 kN) was approximately 17%

488 higher than that of Specimen M2-GR (37.8 kN). These specimens had the same cross-section and

489 reinforcements on the column and Beam A. However, the cross-section of the CEP (200×250 mm^2)

490 on Specimen H3-GR-T200 was larger than that of the beam (200×150 mm^2) of Specimen M2-GR.

491 Therefore, the peak load of Specimen H3-GR-T200 was greater than that of Specimen M2-GR.

492 However, the peak load of Specimen H3-GR-T200 was lower than that with the dry joint D5-SR-S-

493 T200 due to lower prestress forces in the bolts [1] and failure of the filled concrete block (see Sections

494 3.1 and 3.2).

495 As can be seen that the CEP thickness in both hybrid and dry joints significantly affected the loading

496 capacity and DR. For instance, when the thickness of the CEP reduced from 200 mm to 100 mm, the

497 peak load decreased, approximately two times and three times in the hybrid and dry joints,

498 respectively. In addition, the DRs in the push (2.5% DR) and pull (3.5% DR) directions of Specimen

499 H3-GR-T200 were different while those of Specimen H4-GR-T100 were 1.5% DR in both directions.

500 Reducing the CEP thickness in Specimen H4-GR-T100 caused more severe damage to the CEP,

501 whereas the damage of Specimens H3-GR-T200 was governed by the debond failure of the infilled

502 concrete block from the beam which therefore resulted in the unsymmetric push and pull loading

503   capacities (see Figs. 8(c) and 8(d)). As a result, damage in the CEP led to the reduction of the peak

504   load and DR of Specimen H4-GR-T100. For Specimen H3-GR-T200, a combination of damage at

505   the CEP and infilled concrete block led to the reduction of the peak load. A higher DR was observed

506   in the pull direction (3.5% DR) as compared to that in the push direction (2.5% DR). These DRs still

507   reached the requirements for the collapse prevention structural performance level of ASCE 41-17

508   [10] (5% DR). It is because under the standard cyclic loading tests, the joint did not collapse and still

509   had a capacity to resist load when reaching even the drift ratio of 5%, implying the deformation

510   capacity of the joint is sufficient as specified in the design requirement, and also implies the joint has

511   large energy absorption capacity. Therefore, this hybrid joint is a good candidate for use in seismic-

512   prone regions.

513   For dry joints, reducing the CEP thickness to 100 mm on Specimen D6-GR-S-T100 led to a reduction

514   of DR from 3% DR to 1.5% DR. This value (1.5% DR) was consistent with the DR of the previous

515   study by Saqan [51] who reported that this dry joint type showed poor results and it could not be

516   applied in practice. As an effort in improving the performance, this study and the previous studies [1-

517   3, 30] revised the design of this dry joint using FRP bolts, fibre reinforcement, and geopolymer

518   concrete under cyclic and impact loading so that it could be well applied in practice. In general, the

519   CEP thickness is one of the critical parameters that govern the DR and loading capacity of the joints

520   and thus it is intensively investigated in the next section (Section 4.2) for better understanding and

521   optimal design.

4. Numerical simulation with ABAQUS software

523   ABAQUS software was used to build 3D finite element models of the precast beam-column joints

524   connected with GFRP or steel bolts, and GFRP reinforcements. The experimental results of

525   Specimens M2-GR, H4-GR-T100, and D6-GR-S-T100, were used to validate the numerical model.

526   It is because these three specimens fully represented the observed failure modes of the six specimens.

527   After validating the model, an intensive parametric study was conducted to examine the assumptions

528 used in the analytical model of the dry joints in the previous studies [1, 2]. For instance, shear stress

529 primarily concentrated in the middle zone of the CEP and shear failures governed the main failure

530 modes of the dry joints. Also, the effects of the CEP thickness on the dry joints will be investigated

531 in this section. The influence of the CEP thickness on the hybrid joints is relatively similar to that of

532 the dry joints so that it is not presented in this study for brevity.

533 **4.1 Description of the finite element model**

534 The element types, material models, mesh sizes, and contact types will be briefly presented in this

535 section. To reduce the computational cost, the beam-column joints were built symmetrically, as

536 shown in Fig. 15.

537 *4.1.1 Concrete material model*

538 Concrete of the beam-column joints was modelled by eight-node linear brick elements (C3D8). The

539 main failure modes occurred at the joint area and fixed-end (see Fig. 8) so a fine mesh with a size of

540 20 mm was applied in these areas. Meanwhile, a coarse mesh with the size of 40 mm was used for

541 other areas (see Fig 15). It is noted that these mesh sizes were determined based on mesh convergence

542 tests.

543 There are three popular concrete models in ABAQUS including the brittle cracking model, smeared

544 crack model, and concrete damage plasticity model (CDP) [52]. The brittle cracking model and

545 smeared crack model are usually applied for brittle materials (e.g., brittle rocks and plain concrete)

546 under monotonic loading [27] while CDP has been popularly adopted in simulating reinforced-

547 concrete structures under both monotonic and cyclic loading [53]. CDP can well reflect the

548 behaviours of specimens which is governed by concrete with compression failure under cyclic

549 loading. For shear and tensile failures, the application of CDP to simulate the inelastic behaviours of

550 specimens exhibited many limitations [26, 27]. Hence, this study adopts the newly developed

551 softened damage-plasticity model by Feng, et al. [26] and Feng, et al. [54] to simulate behaviours of

552 the reinforced-concrete joints under cyclic loading. The comparison of plain concrete and reinforced

553 concrete under un-softening and softening effects was respectively illustrated in Fig. 16.
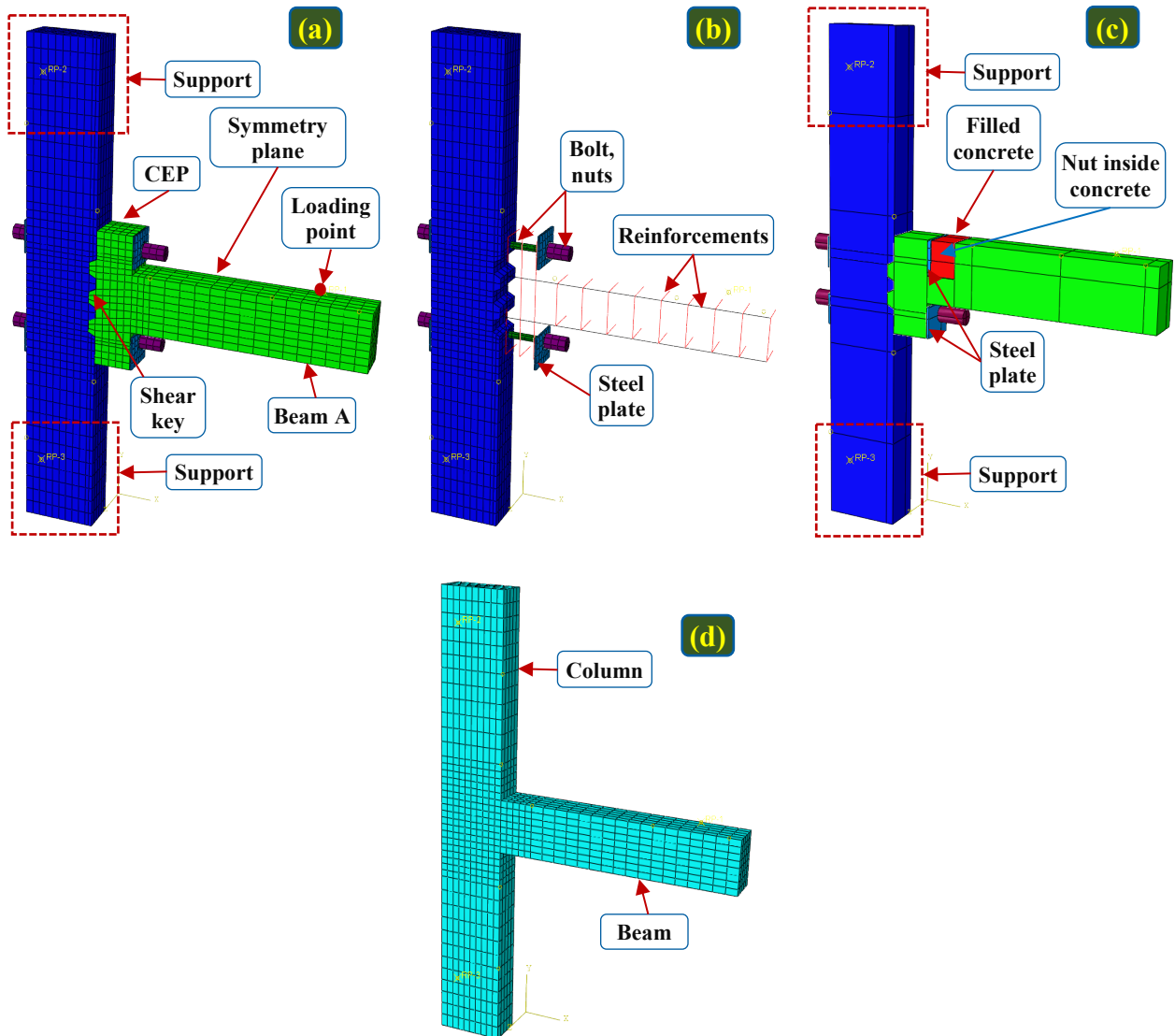
Fig. 15. Main components of the dry and hybrid joints; (a & b) dry joint, (c) hybrid joint, (d) monolithic joint.

556
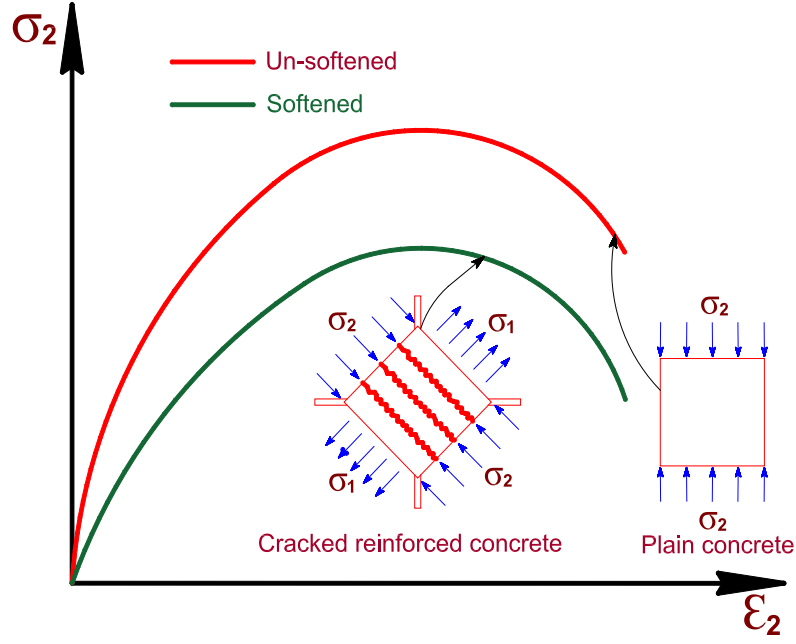
Fig. 16. The effects of compression-softening on reinforced concrete [55].

For brevity, hereafter the concrete material model with the softening effects is briefly introduced. The constitutive relation was represented as:

$$\sigma = (I - D^s) : E_0 : (\epsilon - \epsilon^p) \tag{3}$$

where σ, I, D^s, and E_0 denoted the Cauchy stress tensor, identity tensor, fourth-order damage tensor corresponding to compression-softening, and fourth-order elastic modulus tensor, respectively; ϵ is the strain tensor including two components (elastic part ϵ^e and plastic part ϵ^p); the damage tensor (D^s) is determined as follows:

$$D^s = d^+ P^+ + d^{s-} P^- \tag{4}$$

$$d^{s-} = 1 - \beta(1 - d^-) \tag{5}$$

where P^+ and P^- are the projection tensors; d^+ and d^- indicate the two damage variables of concrete corresponding tensile and compressive performances; β denotes the softening coefficient and is calculated as follows.

$$\beta = \frac{1}{\sqrt{1 + 400 \bar{\epsilon}^{eq+}}} \tag{6}$$

572 It is noted that the softening coefficient is identified based on the tensile energy equivalent strain

573 rather than the principal tensile strain. This model provides more convenience in calculations under

574 complex multi-axial stress state and accounts for the accumulated influence of compression-softening

575 under reverse loading.

576 Moreover, the energy equivalence is proposed by Li and Ren [56] as follows:

$$\bar{\epsilon}^{eq+} = \sqrt{\frac{2Y^+}{E_0}}, \ \bar{\epsilon}^{eq-} = \frac{1}{E_0(1-\alpha)}\sqrt{\frac{Y^-}{b_0}} \tag{7}$$

578 where α and b_0 depend on the material properties; E_0 is the initial elastic modulus [57]; $Y^\pm$ are the

579 damage release rates and are determined as bellow:

$$Y^+ = \frac{1}{2}(\bar{\sigma}^+ : E_0^{-1} : \bar{\sigma}), \ Y^- = b_0(\alpha \bar{I}_1^- + \sqrt{3\bar{J}_2^-})^2 \tag{8}$$

581 where $\bar{I}_1^-$ and $\bar{J}_2^-$ are the first invariant of the compressive effective stress $\bar{\sigma}^-$ and the second invariant

582 of the deviator of the compressive effective stress $\bar{\sigma}^-$, respectively [27].

583 The uniaxial damage evolution functions are determined as follows [54, 58]:

$$d^\pm = \begin{cases} 1 - \frac{\rho^\pm n^\pm}{n^\pm - 1 + (x^\pm)^{n^\pm}} & x^\pm \leq 1 \\ 1 - \frac{\rho^\pm}{\alpha^\pm(x^\pm - 1)^2 + x^\pm} & x^\pm > 1 \end{cases} \tag{9}$$

$$x^\pm = \frac{\bar{\epsilon}^{eq\pm}}{\epsilon_c^\pm}, \ \rho^\pm = \frac{f_c^\pm}{E_0 \epsilon_c^\pm}, \ n^\pm = \frac{1}{1-\rho^\pm} \tag{10}$$

586 where $f_c^\pm$ and $\epsilon_c^\pm$ are the tensile/compressive maximum strength and the corresponding strain; $\alpha^\pm$

587 indicates the descending parameters that govern the shape of the descending part of the stress-strain

588 curves [55].

589 Moreover, ϵ^p is calculated to improve the numerical efficiency of the model, based on the empirical

590 model by Faria, et al. [59] and the modified model by Wu [60].

$$\dot{\epsilon}^p = b^p \bar{\sigma} \tag{11}$$

$$b^p = \xi^p E_0 H(\dot{d}^-) \frac{\langle \epsilon^e : \dot{\epsilon} \rangle}{\bar{\sigma} : \bar{\sigma}} \geq 0 \tag{12}$$

592

593 The plastic coefficient which dominates plastic strain level is denoted by ξ^p. The tensile plastic strain

594 is neglected due to its insignificant effects on the whole structural performance. It is noted that the

595 above model of concrete was implemented into ABAQUS through user-defined subroutine UMAT.

596 *4.1.2 Steel and FRP material models*

597 The GFRP longitudinal reinforcements and stirrups were modelled by truss elements (T3D2) while

598 C3D8 was used to model the bolts and steel plates. After conducting the mesh convergence tests, the

599 20-mm mesh size was applied for these elements. Material properties of GFRP bolts and GFRP

600 reinforcements are presented in Tables 3 and 4. The anisotropic elastic material model was applied

601 for all GFRP bolts and GFRP reinforcements in this study owing to the linear performance of GFRP

602 material till failure. For steel bolts and steel plates, the elastoplastic stress-strain material model was

603 used [25].

604 *4.1.3 Contact mechanism*

605 The perfect bond between reinforcement and concrete was adopted in the numerical simulation. It is

606 because there was no slippage between reinforcement and concrete observed in the tests. In addition,

607 previous studies [7, 25, 53, 61] also proved that using a perfect bond model can give reasonable

608 predictions of the behaviours of the structures. Therefore, embedded elements were adopted in the

609 numerical model to define contact between the reinforcements and concrete. The surface-to-surface

610 contact was applied between two shear key surfaces of the beam and column with a friction coefficient

611 of 0.7 [25]. The spacing between the bolts and the holes on the beams and columns of dry and hybrid

612 joints was respectively 4 mm and 1.5 mm so the unbonded contact was adopted. Zero friction was

613 assumed in unbonded contact to define the tangential behaviour between the bolts and the holes [25].

614 Tie constraint contact was applied between steel plate and CEP/column surfaces and between nut and

615 steel plate surfaces. In addition, to maintain affordable computational cost (simulation time) but keep

616 the same accuracy as using the other available contact types, the tie constraint contact was adopted

617 between the filled concrete and old concrete/steel plate surfaces.

618 *4.1.4 Model validation and discussions*

619 Using ABAQUS to simulate the performance of reinforced-concrete structures with shear and tensile

620 failures under cyclic loading is challenging due to the limitation of the concrete model as reported in

621 the previous studies [26, 27]. Hence, only the loading-displacement relationship under the monotonic

622 loading was simulated instead of the cyclic loading in previous studies [7, 28, 29]. This study shows

623 an improvement compared to the previous studies [7, 28, 29] because the performances of the dry

624 and hybrid joints under cyclic loading could be well simulated till the peak loads. The peak load point

625 was defined at the corresponding loading value when concrete or reinforcements reached their

626 maximum stress or yield strength. However, inconsistent numerical results under cyclic loading

627 conditions in the post-peak region were observed owing primarily to the incapability of the material

628 model to properly represent the post-failure performance of the concrete material under complex

629 stress states induced by combined bending moment and shear force. Owing to this limitation, and also

630 because the stress distribution and damage of materials up to the peak loads are the primary concern

631 in the analysis and design of a beam-column joint, and also the primary focus of this investigation, in

632 this study, like in the previous studies [7, 28, 29], simulation of the structural performance under

633 monotonic loading is also carried out to obtain the loading-displacement envelope. Hence, this study

634 uses both hysteretic curves under cyclic loading up to the peak load and envelope curves under

635 monotonic loading to validate the accuracy of the numerical simulation results. Afterwards, only the

636 numerical simulation under monotonic loading, which was computationally a lot more efficient

637 compared to simulations under cyclic loading, was applied to conduct parametric investigations. The

638 values of the ductility, DR, and loading capacity of the proposed dry and hybrid joints could be used

639 to evaluate the performance of these joints when applying in seismic-prone areas. The ED derived

640 from the results of the numerical simulation depends on the concrete constitute model and its ability

641   to represent concrete material behaviour in the post-failure region under complex stress states, which

642   is a good topic for future studies.

643   The numerical model was validated with the experimental results in terms of hysteretic loops,

644   envelope curves, and failure modes, as shown in Figs. 17 and 18. Only the first cycle of each DR

645   level (2 cycles in the experiment) was applied in the numerical simulation to reduce the simulation

646   time. The envelope curve of Specimen H4-GR-T100 was plotted in both push and pull directions due

647   to the asymmetric design of this specimen. In general, the numerical simulation well captured the

648   peak loads, DR, and the stiffness of the monolithic and dry joints. The differences in numerical results

649   and experimental peak loads ranged between 4.1% and 6.7%. For example, the experimental peak

650   load of Specimen D6-GR-S-T100 was 16.8 kN while the corresponding numerical result under cyclic

651   and monotonic loading was 17.5 kN and 17.9 kN, respectively. However, the unloading curves of the

652   numerical simulation do not match well with the experimental results, as shown in the red curve of

653   Fig. 17 (a). This limitation is attributed to the concrete model as discussed above. Multiple cycles

654   were applied in each level of DR in the experimental test while only one cycle at each DR was carried

655   out in the numerical simulation to save computation time as also adopted in a previous study [55].

656   This difference might further contribute to the variation between the numerical and experimental

657   results. This limitation was also reported in previous studies [6, 27, 62-64] and thus improving the

658   concrete model that takes into consideration the load-path effect is deemed necessary, particularly for

659   unloading curves.
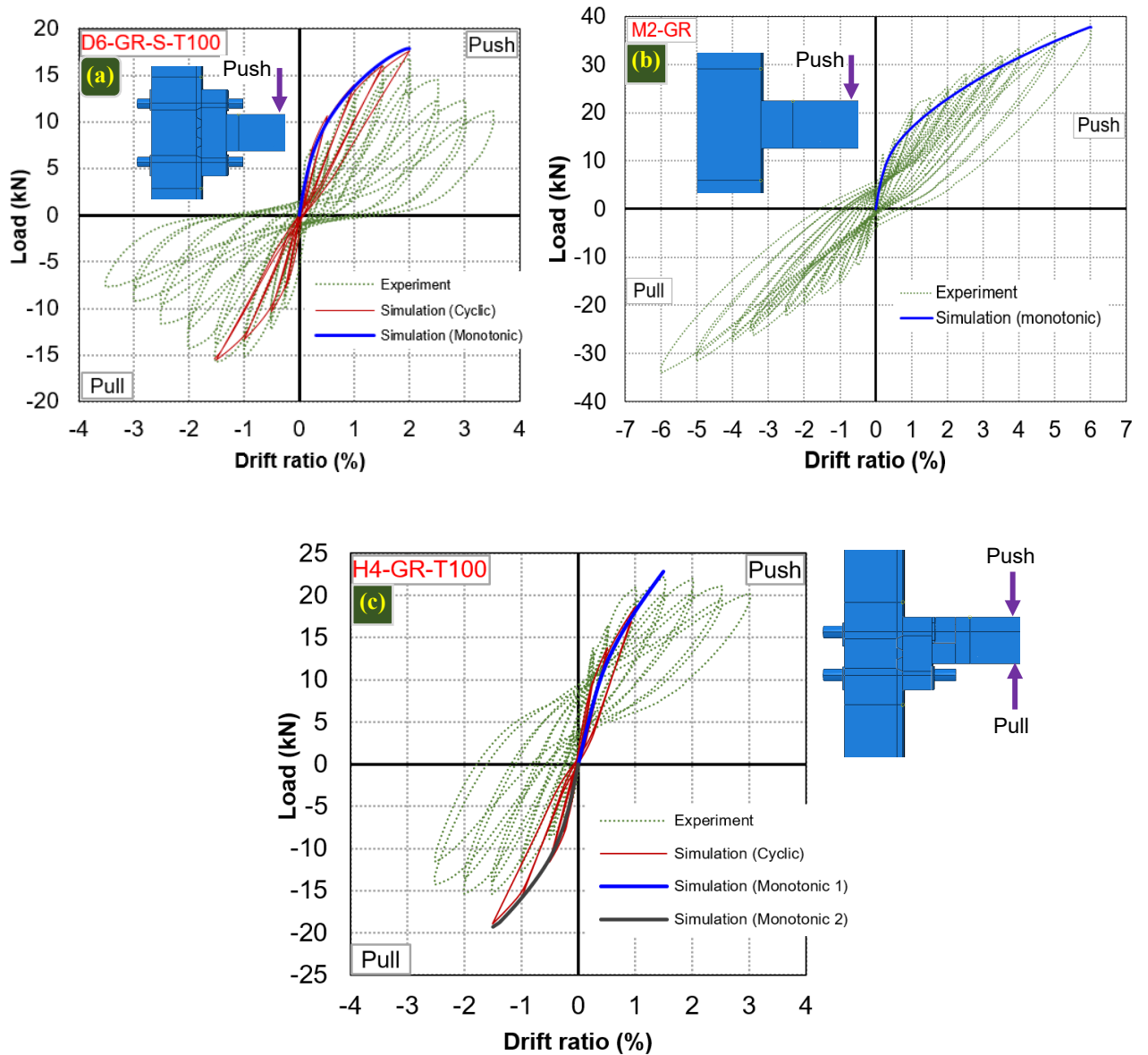
Note: Monotonic 1 and monotonic 2 are plotted in the push and pull directions, respectively.

**Fig. 17.** Comparison of hysteretic and envelope curves between experiment and numerical simulation results.

Although the numerical model successfully predicted the peak load in the push direction of the hybrid joint, a higher variation (approximately 24%) was observed in the pull direction, as shown in Fig. 17(c). This result is attributed to the contact between the old and new concrete surfaces used in the numerical simulation model. This study adopted the tie constraint contact to simulate the contact between the old and new concrete surfaces, which did not well reflect the real contact as observed in the test. Unfortunately, no information regarding the mechanical properties of such contact is

669   available in the literature. The contact between old and new concrete of different strengths needs to

670   be improved in further studies. In addition, the simulations of hysteretic curves of Specimens D6-

671   GR-S-T100 and H4-GR-T100 were stopped at the peak load with 2% and 1.5% DR, respectively, as

672   shown in Figs. 17(a) and 17(c) because running the full hysteretic curves was computationally very

673   intensive, and also because of the limitation of the current concrete material model which does not

674   necessarily yield good post-failure representations as discussed above.
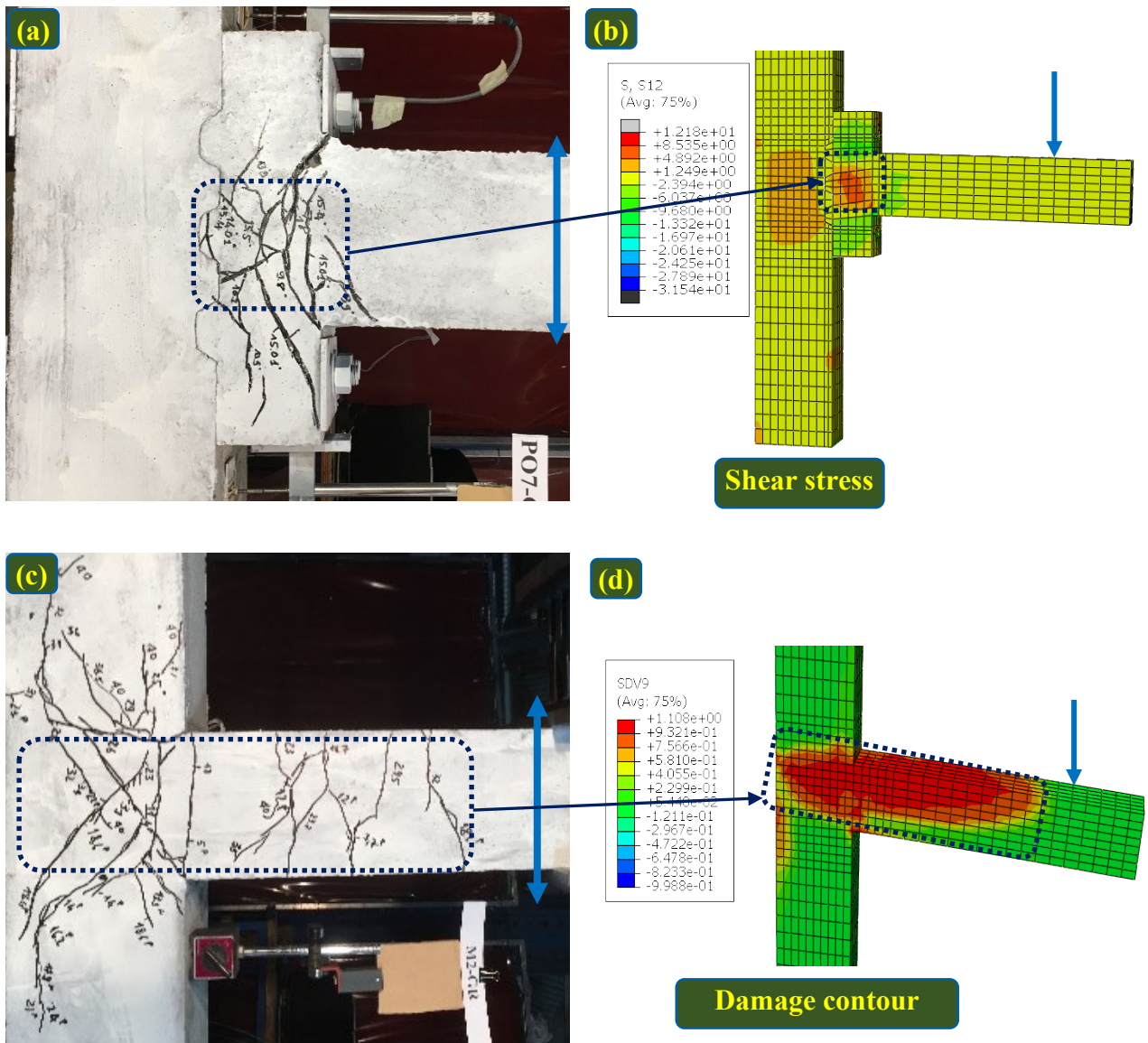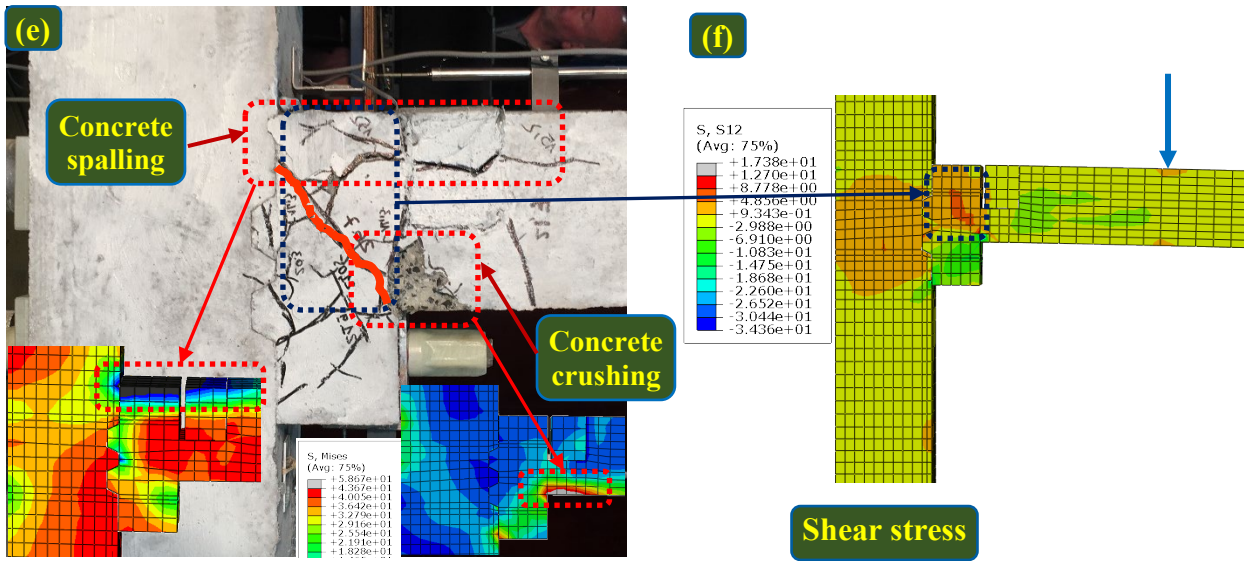
Fig. 18. Comparison of failure modes between experiment and numerical simulation of Specimens D6-GR-S-T100 (a-b), M2-GR (c-d), and H4-GR-T100 (e-f) at the peak load (unit: MPa).
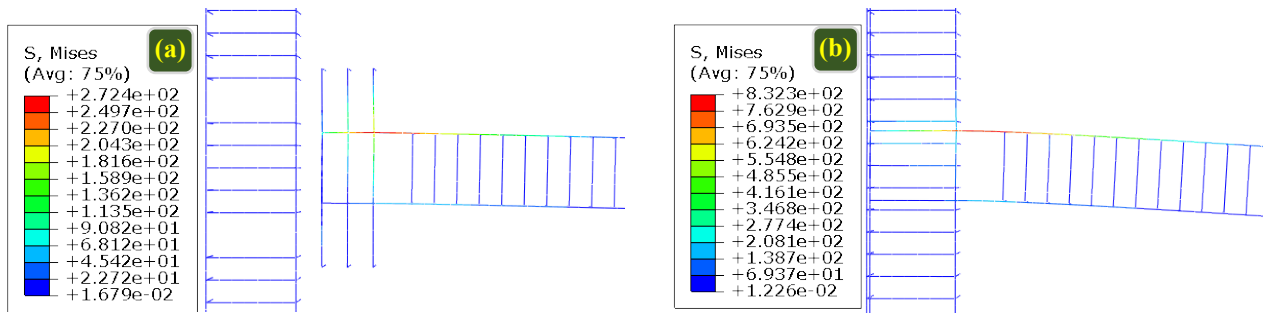
Fig. 19. Tensile stress in GFRP reinforcements: (a) dry joint and (b) monolithic joint (unit: MPa).

It can be seen in Figs. 18(a) and 18(b) that the numerical model successfully captured the failure patterns of the dry joint D6-GR-S-T100. In the experimental results, the cracks mainly developed in the middle joint of the CEP while there were no visible cracks at the top and bottom zones. The data of strain gauges in the previous studies [1, 3] illustrated that shear and tensile cracks governed the main failure of this type of dry joint. This finding was consistent with the data from the numerical model, as shown in Fig. 18(b). It can be seen from the numerical results that shear stress firstly occurred in the middle zone of the CEP and then they extended. The tensile stress of GFRP stirrups and longitudinal reinforcements did not reach their nominal tensile strength (approximately 1,259 MPa), as shown in Fig. 19(a). It means the shear failure of concrete in the middle zone of CEP

688   governed the main failure of the dry joint (D6-GR-S-T100). This result is different from the findings

689   of the previous studies [51, 65] which adopted the model of the monolithic joint for the precast joint

690   and concluded that the strut-tie failure governed the main failure of this type of dry joint.

691   For the monolithic specimen, the damage contours of the numerical model also well predicted the

692   failure modes of the monolithic specimen (M2-GR), as shown in Figs. 18(c) and 18(d). More severe

693   damage was observed in the joint area and at the fixed-end of the beam due to the shear stress and the

694   bending stress/concrete crushing, respectively. In addition, since the tensile stress of the GFRP

695   reinforcements in the specimens did not reach their nominal tensile strength (see Fig. 19(b)), concrete

696   governed the main failure modes of both the monolithic and dry joints.

697   Similar to the dry and monolithic joints, the concrete failure is the primary failure mode of the hybrid

698   joints. The numerical model also successfully captured the failure patterns of Specimen H4-GR-T100,

699   as shown in Figs. 18(e) and 18(f). The inclined cracks appeared in the joint area due to the shear stress

700   as illustrated in Fig 18(f). In addition, the numerical results indicated that the concentrated

701   compressive stress caused the concrete crushing at the fix-end and the concrete spalling at the bottom

702   zone of the CEP (see Fig 18(e)). For instance, the maximum compressive stress of concrete at the

703   fixed-end was 58.8 MPa which reached the compressive strength of concrete (59.1 MPa). The results

704   of numerical simulations are consistent with the observed failures of the hybrid joint in Section 3.1.

705   **4.2 Effect of concrete-end-plate thickness**

706   The above comparisons between experiment and numerical simulation results have proven the

707   reliability of the numerical model and thus it is used to examine the effects of the CEP thickness on

708   the structural behaviour. The model of Specimen D6-GR-S-T100 was used as a reference dry beam-

709   column joint. Numerical models of six specimens which had a similar design but different CEP

710   thicknesses were built based on the model of the reference specimen. The thickness of the CEP was

711   chosen based on the height of the beam section. The numerical model of the tested specimen D6-GR-

712 S-T100 was named as D7-T100, and the new numerical models with other CEP thicknesses were

713 named accordingly as detailed in Table 7.

714 **Table 7.** Description of specimens built on ABAQUS.

Name	Thickness (mm)	CEP/Beam	Reinforcements	Bolts	Axial forces (kN)	Prestress forces (kN)
D7-T100	100	0.7	GFRP	Steel	65	35
D8-T150	150	1	GFRP	Steel	65	35
D9-T200	200	1.3	GFRP	Steel	65	35
D10-T250	250	1.7	GFRP	Steel	65	35
D11-T300	300	2	GFRP	Steel	65	35
D12-T350	350	2.3	GFRP	Steel	65	35

715 Note*:* D7-T100 is the numerical model of D6-GR-S-T100.

716 *4.2.1 Failure modes*

717 Fig. 20 shows the shear stress distribution of the dry joints with different CEP thicknesses. Only the

718 failure modes of Specimens D7-T100, D9-T200, D11-T300, and D12-T350 were representatively

719 shown in this figure for brevity, as shown in Fig. 20. In general, the failure mode of the dry joint was

720 shifted from the CEP area (Specimen D7-T100) to the beam at the fixed-end (Specimen D9-T200)

721 when increasing the CEP thickness. However, if the CEP thickness was further increased, the failure

722 model changed again from the beam to the column (Specimen D11-T300). For example, the shear

723 failure in the middle zone of the CEP was the primary failure modes of Specimen D7-100 (see Fig.

724 20). When the CEP thickness increased from 100 to 200 mm, the shear stress in the middle zone of

725 Specimen D9-T200 was reduced as compared to Specimen D7-T100 due to increasing the thickness

726 of this section. The flexural failure and concrete crushing at the fixed-end of the beam became the

727 primary failure modes of Specimen D9-T200. This result was consistent with the failure mode of

728 Specimen PS4 reported in the previous study [3]. When the CEP thickness was 300 mm or more, the

729 failure shifted to the column. As can be seen clearly in Figs. 20(D11-T300) and 20(D12-T350), higher

730 shear stress was observed on the column, compared to the CEP. This shear stress caused severe

731 damage on the column while almost no shear damage was recorded on the CEP. It means that if the

732 CEP thickness was sufficiently large, compared to the section's height of the beam and the column,

733 the design principle of the strong column-weak beam may not be satisfied. Therefore, the CEP

734 thickness needs to be carefully chosen in the design process to avoid making the column the weaker

735 component in the structure.
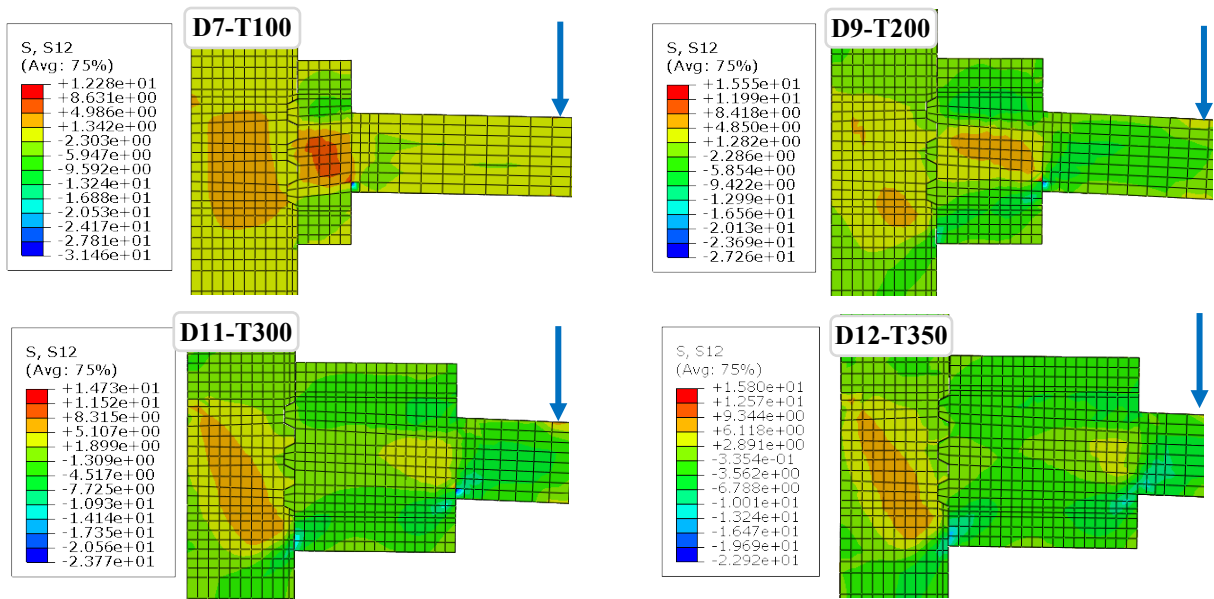
736 **Fig. 20.** Shear stress distribution on dry joints with different CEP thickness (unit: MPa).

737 Fig. 21 illustrates the principal compressive stress flow of the typical specimens. The distribution of

738 all compressive, tensile and shear stresses in the CEP of the dry joint was very complicated. Fig. 21

739 only shows stress flow of the compressive stress for demonstration. The compressive stress in the

740 middle zone of the CEP was quite small which did not reach the compressive strength of concrete.

741 Therefore, there was no compressive strut failure as suggested in the previous studies [51, 65]. For

742 instance, the maximum compressive stress of concrete in the middle zone of Specimens D7-100 and

743 D9-200 was 16 MPa and 19 MPa (see Figs 21(D7-T100) and 21(D9-T200)), respectively which is

744 significantly lower than the compressive strength of concrete (38.5 MPa). Hence, the compression

745 strut failure did not occur in these specimens. In addition, high compressive stress was observed in

746 the top and bottom zone of the CEP due to the effect of the prestress forces of the bolts. Steel spirals

46

747 were utilized in these locations in the previous study [3] but the capacities of the dry joint were not

748 improved because the failure was not governed by compressive concrete at these regions either. The

749 compressive stress in the top and bottom zones of CEP (e.g., 26 MPa in Specimen D9-T200) was

750 lower than the nominal compressive strength of concrete. This finding explains why steel spirals were

751 not useful in this case. For the compressive stress flow on the column of dry joints, the stress

752 distribution was observed as in the joint area of the monolithic joint. A compressive strut was

753 generated in the column of the dry joint due to the compressive forces at the anchor of the bolts and

754 at the bottom left of CEP, as illustrated in Fig. 21. Interestingly, when the CEP thickness reached 300

755 mm, the direction of stress flow altered with no compressive strut in the middle zone of CEP due to

756 changing the failure mode from the beam to the column.
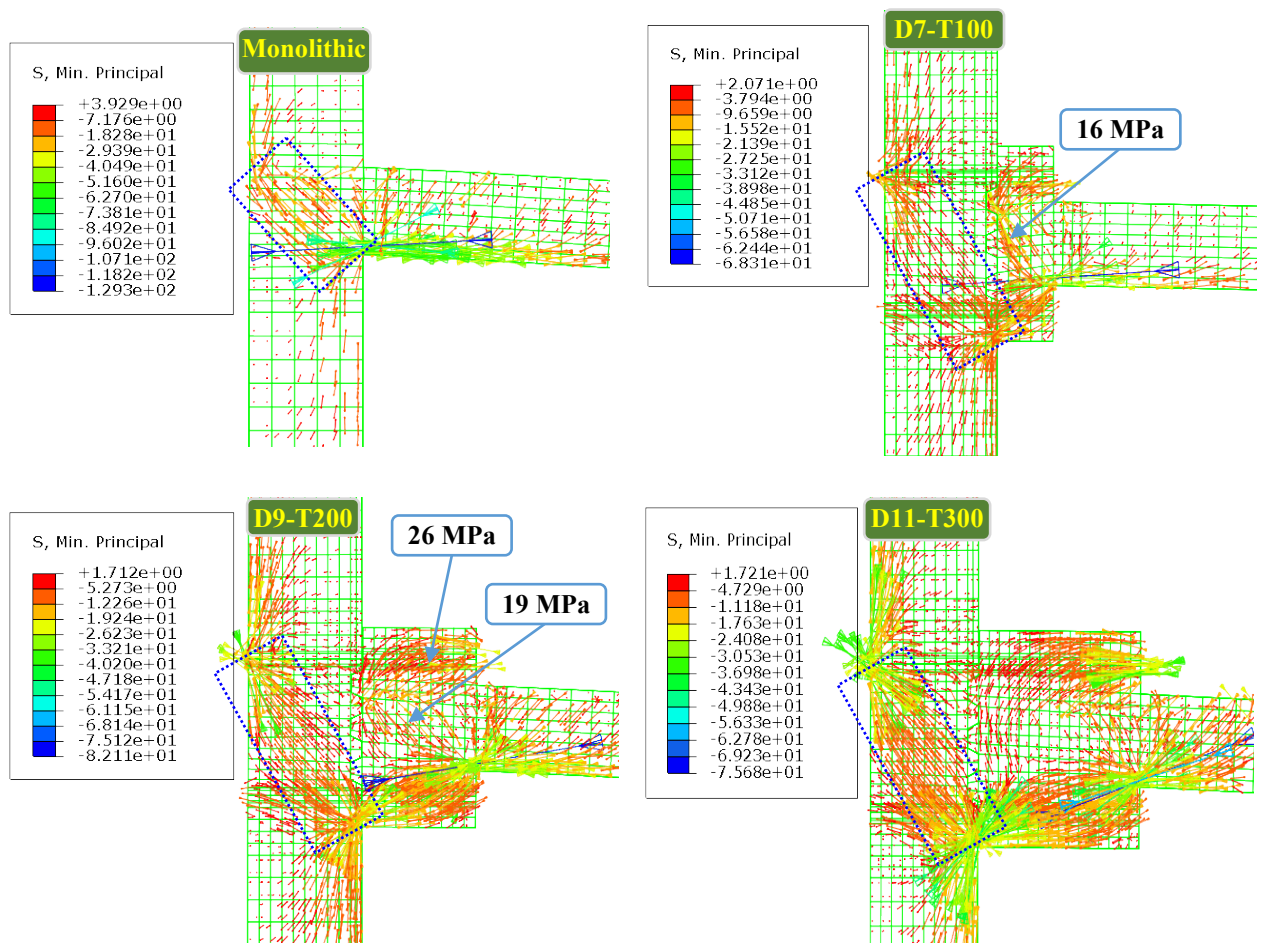
757 **Fig. 21.** Principal compressive stress flow (unit: MPa).

758

759   *4.2.2 Peak load and drift ratio*

760   The CEP thickness significantly affects both the peak load and DR (see Fig. 22). As mentioned in the

761   introduction section, this dry joint was proposed based on the previous study of Saqan [51] who

762   reported that its DR and energy absorption were inadequate. The 1.5% maximum DR value recorded

763   in the previous study [51] was consistent with DR of Specimen D6-GR-S-T100 in the pull direction.

764   In the first stage of our project, the CEP thickness was intentionally increased up to 200 mm, which

765   was thicker than the CEP thickness of Specimen DB-TC in Saqan [51]. As a result, the maximum DR

766   increased from 1.5% to 3.0% as reported in the authors' previous studies [1, 3, 19], which satisfied

767   the requirements of many standards (e.g., ASCE 41-17 [10] and CSA A23.3-07 [11]) for using in

768   seismic-prone areas. The DR of Specimen D9-T200 (3.5%) in the numerical simulation was slightly

769   higher than the result of the previous studies (3%) [3, 14] because GFRP reinforcements were used

770   to replace steel reinforcements which led to an increase of the DR, as explained in the monolithic

771   specimen of the above section (Section 3.4).
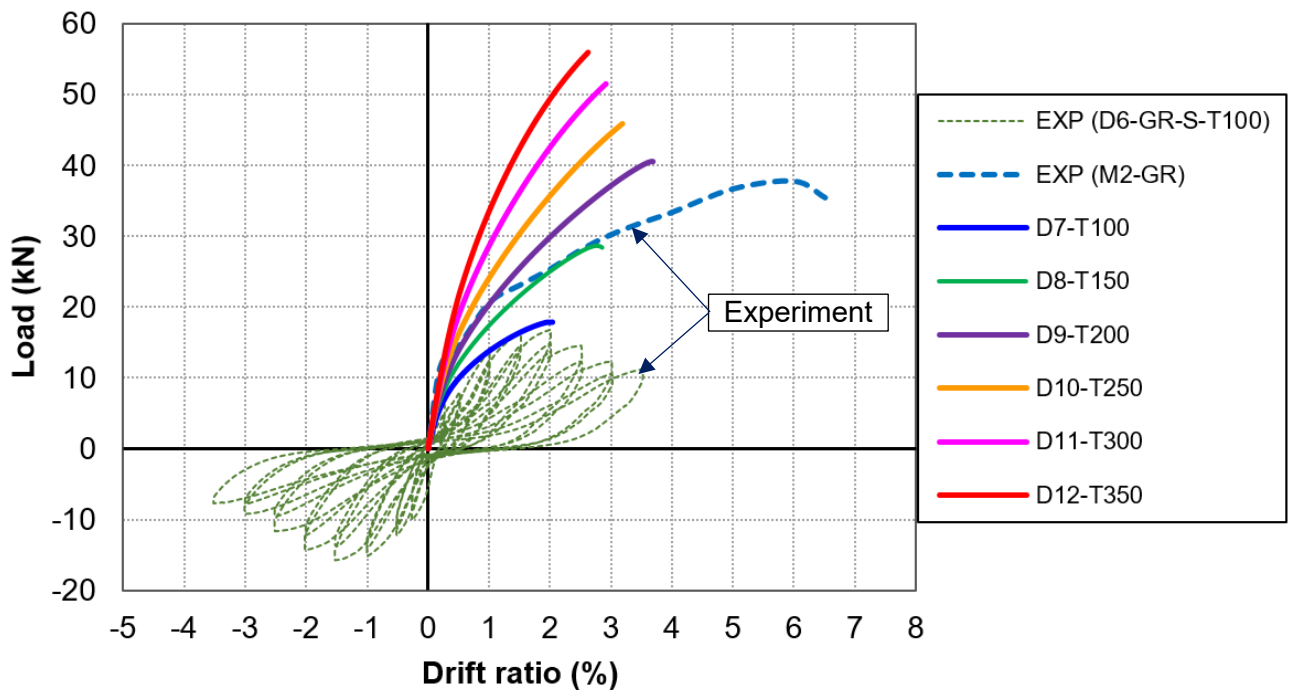
772

773   **Fig. 22.** Comparison of the peak load and drift ratio.

774

775 As mentioned in the previous section, increasing the thickness of the CEP results in improved

776 performance of the precast joint, but further increasing the CEP thickness may lead to an adverse

777 effect. As indicated in Fig. 22, there was an optimal value of the CEP thickness of approximately 200

778 mm. Based on the numerical results, the ratio of CEP/Beam= 1.3 (200-mm CEP thickness) was the

779 optimal value of the dry joint in this study. For instance, Specimen D9-T200 reached 3.5% DR while

780 increasing the CEP thickness up to 250, 300, and 350 mm caused a reduction of DR to 3.2%, 2.9%,

781 and 2.6%, respectively. This reduction is attributed to changing of the failure modes from the joint

782 and the beam to the column because the CEP made the beam and joint strong. The peak loads of the

783 precast joints increased with the CEP thickness. For example, when the CEP thickness was increased

784 from 100 mm to 150, 200, 250, 300, and 350 mm, the peak load also steadily increased from 17.8 kN

785 to 28.5, 40.3, 45.7, 51.1, and 55.3 kN, respectively. Meanwhile, both the peak load and ductility need

786 to be considered in the structural design under seismic loading. If a structure achieves a very high

787 peak load but shows a brittle failure, it is not suitable for use in seismic-prone regions. Based on this

788 perspective, the dry joint with the 200-mm CEP thickness was the best option in this study because

789 it achieved the highest DR, compared to other dry joints. Moreover, the peak load of Specimen D9-

790 T200 (40.3 kN) was higher than that of the corresponding monolithic joint M2-GR (37.8 kN) as

791 shown in Fig. 22. Therefore, the thickness ratio of CEP/Beam= 1.3 could be considered in the design

792 of this dry joint type. More studies are deemed necessary to enhance the understanding and further

793 confirm this suggestion.

794 **5. Conclusions**

795 A new hybrid joint was proposed in this study to improve the design of the dry beam-column joint

796 with a bulky CEP. The performances of the hybrid and dry joints were experimentally and

797 numerically investigated. The main findings can be summarised as follows:

798   1. The hybrid joint showed sufficient capacities, compared to the monolithic joint. The energy

799   dissipation and the peak load of the hybrid joint were approximately 57% and 17% higher than the

800   reference monolithic joint, respectively.

801   2. Based on the experimental and numerical simulation results, the CEP thickness significantly

802   affects the dry and hybrid joint performances, such as failure mode, DR, peak load, and ED. In

803   addition, the numerical simulation results suggested that the thickness ratio of CEP/Beam= 1.3 was

804   an optimal value of the CEP thickness which could be considered in the design of this dry joint type.

805   3. GFRP bolts and reinforcements could replace the steel bolts and reinforcements to mitigate

806   corrosion damage. The application of GFRP in this study provided not only ductile failure but also

807   the great centring capability (smaller residual displacement).

808   4. The application of the modified concrete model well captured the failure mode up to the peak

809   load and the peak load of the precast joint with a marginal variation of 4.1-6.7%.

810   5. The numerical simulation results illustrated that the shear and tensile stress in the middle

811   zone of CEP mainly governed the joint failure of the dry joint. Therefore, the assumption in the

812   analytical model of the previous study [1, 2] was numerically confirmed.

813   In conclusion, this study proposes an alternative for designing precast concrete structures which could

814   not only reduce the construction cost but also offer more convenience in applying new technology

815   into the construction sector.

Author contribution

Tuan T. Ngo: Data curation, Formal analysis, Investigation, Methodology, Software, Validation, Visualization, Writing - original draft.

Thong M. Pham: Methodology, Project administration, Supervision, Writing - review & editing.

Hong Hao: Funding acquisition and project chief investigator, Supervision, Research direction and scope definition, Writing - review & editing.

Wensu Chen: Supporting the experimental process, Resources.

Ngoc San Ha: Software, Validation.

Compliance with ethical standards

Conflict of interest

The authors declare that they have no conflict of interest.

837   **References**

838   [1] T.T. Ngo, T.M. Pham, H. Hao, Effects of steel fibres and prestress levels on behaviour of newly
839   proposed exterior dry joints using SFRC and CFRP bolts, Eng. Struct. 205 (2020) 110083.
840   [2] T.T. Ngo, T.T. Tran, T.M. Pham, H. Hao, Performance of geopolymer concrete in monolithic and
841   non-corrosive dry joints using CFRP bolts under cyclic loading, Compos. Struct. (2020) 113394.
842   [3] T.T. Ngo, T.M. Pham, H. Hao, Ductile and dry exterior joints using CFRP bolts for moment-
843   resisting frames, Structures 28 (2020) 668-684.
844   [4] M. Saatcioglu, Cracking in concrete structures during the August 17, 1999 earthquake in Turkey,
845   ACI-Special Publication 204 (2001) 261-276.
846   [5] M.N.S. Hadi, T.M. Tran, Retrofitting nonseismically detailed exterior beam–column joints using
847   concrete covers together with CFRP jacket, Constr. Build. Mater. 63 (2014) 161-173.
848   [6] L. Chu, Y. Tian, D. Li, Y. He, H. Feng, Shear behavior of steel reinforced concrete column-steel
849   beam joints with or without reinforced concrete slab, J. Build. Eng. 35 (2021) 102063.
850   [7] H. Dabiri, A. Kaviani, A. Kheyroddin, Influence of reinforcement on the performance of non-
851   seismically detailed RC beam-column joints, J. Build. Eng. 31 (2020) 101333.
852   [8] Y. Murad, Joint shear strength models for exterior RC beam-column connections exposed to
853   biaxial and uniaxial cyclic loading, J. Build. Eng. 30 (2020) 101225.
854   [9] A. Maddah, A. Golafshar, M.H. Saghafi, 3D RC beam–column joints retrofitted by joint
855   enlargement using steel angles and post-tensioned bolts, Eng. Struct. 220 (2020) 110975.
856   [10] ASCE 41-17, Seismic rehabilitation of existing buildings, ASCE 41-17, ASCE, ASCE Reston,
857   VA, 2017.
858   [11] CSA A23.3-07, Design of concrete structures, CSA A23.3-07, CSA (Canadian Standards
859   Association), Mississauga, Ontario, 2007.
860   [12] N. Alver, M.E. Selman, O.B. Akgun, The effect of short cantilever beam formation on the
861   structural behavior of precast post-tensioned connections, Constr. Build. Mater. 35 (2012) 232-239.
862   [13] K. Jin, K. Kitayama, S. Song, K.-o. Kanemoto, Shear capacity of precast prestressed concrete
863   beam-column joint assembled by unbonded tendon, ACI Struct. J. 114(1) (2017) 51.
864   [14] T.T. Ngo, T.M. Pham, H. Hao, Use of CFRP bolts in dry beam-column joints for sustainable
865   prefabrication constructions, APFIS2019, Surfers Paradise, Gold Coast, Australia, 2019.
866   [15] D. Guan, H. Yang, D. Ju, Z. Guo, S. Yang, Cyclic loading test on a locally post-tensioned precast
867   concrete beam–column connection, Adv. Struct. Eng. 22(12) (2019) 2699-2711.
868   [16] H. Wang, E.M. Marino, P. Pan, H. Liu, X. Nie, Experimental study of a novel precast prestressed
869   reinforced concrete beam-to-column joint, Eng. Struct. 156 (2018) 68-81.
870   [17] W. Xue, B. Zhang, Seismic behavior of hybrid concrete beam-column connections with
871   composite beams and cast-in-place columns, ACI Struct. J. 111(3) (2014) 617-627.
872   [18] X. Yan, S. Wang, C. Huang, A. Qi, C. Hong, Experimental study of a new precast prestressed
873   concrete joint, Applied Sciences 8(10) (2018) 1871.
874   [19] H. Hao, T.T. Ngo, T.M. Pham, Performance of dry exterior beam-column joints using CFRP
875   bolts and SFRC under cyclic loading, Australian Earthquake Engineering Society 2019 Conference,
876   Newcastle, NSW, Australia, 2019.
877   [20] M. Kaya, A.S. Arslan, Analytical modeling of post-tensioned precast beam-to-column
878   connections, Mater. Des. 30(9) (2009) 3802-3811.
879   [21] P. Alaee, B. Li, Analytical Investigations of Reinforced Concrete Beam–Column Joints
880   Constructed Using High-Strength Materials, J. Earthquake Eng. 24(5) (2020) 774-802.
881   [22] S.A. Kulkarni, B. Li, W.K. Yip, Finite element analysis of precast hybrid-steel concrete
882   connections under cyclic loading, J. Constr. Steel Res. 64(2) (2008) 190-201.
883   [23] B. Li, S.A. Kulkarni, C.L. Leong, Seismic Performance of Precast Hybrid-Steel Concrete
884   Connections, J. Earthquake Eng. 13(5) (2009) 667-689.

885 [24] A. Mosallam, K. Allam, M. Salama, Analytical and numerical modeling of RC beam-column
886 joints retrofitted with FRP laminates and hybrid composite connectors, Compos. Struct. 214 (2019)
887 486-503.
888 [25] T.D. Le, T.M. Pham, H. Hao, Numerical study on the flexural performance of precast segmental
889 concrete beams with unbonded internal steel tendons, Constr. Build. Mater. 248 (2020) 118362.
890 [26] D.-C. Feng, X.-D. Ren, J. Li, Softened damage-plasticity model for analysis of cracked
891 reinforced concrete structures, J. Struct. Eng. 144(6) (2018) 04018044.
892 [27] D.-C. Feng, X.-D. Ren, J. Li, Cyclic behavior modeling of reinforced concrete shear walls based
893 on softened damage-plasticity model, Eng. Struct. 166 (2018) 363-375.
894 [28] Y.B. Abu Tahnat, M.M.S. Dwaikat, M.A. Samaaneh, Effect of using CFRP wraps on the strength
895 and ductility behaviors of exterior reinforced concrete joint, Compos. Struct. 201 (2018) 721-739.
896 [29] S. Bahrami, M. Madhkhan, F. Shirmohammadi, N. Nazemi, Behavior of two new moment
897 resisting precast beam to column connections subjected to lateral loading, Eng. Struct. 132 (2017)
898 808-821.
899 [30] T.T. Ngo, T.M. Pham, H. Hao, W. Chen, M. Elchalakani, Performance of monolithic and dry
900 joints with GFRP bolts reinforced with different fibres and GFRP bars under impact loading, Eng.
901 Struct. 240 (2021) 112341.
902 [31] ACI T1.1-01, Acceptance criteria for moment frames based on structural testing and
903 commentary, ACI T1.1-01, ACI Committee, American Concrete Institute, 2001, pp. 1-7.
904 [32] Boral Pty Ltd, https://www.boral.com.au/, Australia, 2020.
905 [33] AS 1012.8.1-14, Method for making and curing concrete-compression and indirect tensile test
906 specimens, AS 1012.8. 1-14, AS (Australian Standard), Sydney, NSW, 2014.
907 [34] AS 1012.9.1-14, Methods of testing concrete-compressive strength tests-concrete, mortar and
908 grout specimens, AS 1012.9.1-14, AS (Australian Standard), Sydney, NSW, 2014.
909 [35] S.S. Mahini, H.R. Ronagh, Web-bonded FRPs for relocation of plastic hinges away from the
910 column face in exterior RC joints, Compos. Struct. 93(10) (2011) 2460-2472.
911 [36] M. Hasaballa, E. El-Salakawy, Shear capacity of exterior beam-column joints reinforced with
912 GFRP bars and stirrups, J. Compos. Constr. 20(2) (2015) 04015047.
913 [37] R. Rahman, S. Dirar, Y. Jemaa, M. Theofanous, M. Elshafie, Experimental behavior and design
914 of exterior reinforced concrete beam-column joints strengthened with embedded bars, J. Compos.
915 Constr. 22(6) (2018) 04018047.
916 [38] Bluey Pty Ltd, Https://www.bluey.com.au/category/blugeo, 2020. http://texo.net.au/.
917 [39] Pultrall Inc, Https://www.fiberglassrebar.com/, Canada, 2020.
918 [40] ACI 318-11, Building code requirements for structural concrete and commentary, ACI 318-11,
919 ACI (American Concrete Institute), Farmington Hills, MI 48331, 2011, p. 503.
920 [41] ACI 440.1R-15, Guide for the design and construction of structural concrete reinforced with
921 FRP bars, ACI 440.1R-06, American Concrete Institute, 2015.
922 [42] ACI 374.1-05, Acceptance criteria for moment frames based on structural testing and
923 commentary, ACI 374.1-05, ACI (American Concrete Institute), Farmington Hills, MI, 2005, p. 9.
924 [43] L. Palmieri, E. Saqan, C. French, M. Kreger, Ductile connections for precast concrete frame
925 systems, ACI-Special Publication 162-13 (1996) 313-356.
926 [44] D. Mostofinejad, A. Akhlaghi, Flexural strengthening of reinforced concrete beam-column joints
927 using innovative anchorage system, ACI Struct. J. 114(6) (2017) 1603-1614.
928 [45] M. Kaya, A. Samet Arslan, The effect of the diameter of prestressed strands providing the post-
929 tensioned beam-to-column connections, Mater. Des. 30(7) (2009) 2604-2617.
930 [46] S. Alavi-Dehkordi, D. Mostofinejad, P. Alaee, Effects of high-strength reinforcing bars and
931 concrete on seismic behavior of RC beam-column joints, Eng. Struct. 183 (2019) 702-719.
932 [47] S.K. Ghomi, E. El-Salakawy, Effect of joint shear stress on seismic behaviour of interior GFRP-
933 RC beam-column joints, Eng. Struct. 191 (2019) 583-597.

934 [48] J. Shafaei, A. Hosseini, M.S. Marefat, Seismic retrofit of external RC beam–column joints by
935 joint enlargement using prestressed steel angles, Eng. Struct. 81 (2014) 265-288.
936 [49] S.K. Ghomi, E. El-Salakawy, Seismic performance of GFRP-RC exterior beam–column joints
937 with lateral beams, J. Compos. Constr. 20(1) (2016) 04015019.
938 [50] M. Mady, A. El-Ragaby, E. El-Salakawy, Seismic behavior of beam-column joints reinforced
939 with GFRP bars and stirrups, J. Compos. Constr. 15(6) (2011) 875-886.
940 [51] E.I. Saqan, Evaluation of ductile beam-column connections for use in seismic- resistant precast
941 frames, Faculty of the graduate school, University of Texas at Austin, USA, 1995.
942 [52] J. Lubliner, J. Oliver, S. Oller, E. Oñate, A plastic-damage model for concrete, Int. J. Solids
943 Struct. 25(3) (1989) 299-326.
944 [53] C. Li, H. Hao, K. Bi, Numerical study on the seismic performance of precast segmental concrete
945 columns under cyclic loading, Eng. Struct. 148 (2017) 373-386.
946 [54] D.-C. Feng, G. Wu, Z.-Y. Sun, J.-G. Xu, A flexure-shear Timoshenko fiber beam element based
947 on softened damage-plasticity model, Eng. Struct. 140 (2017) 483-497.
948 [55] D.-C. Feng, G. Wu, Y. Lu, Finite element modelling approach for precast reinforced concrete
949 beam-to-column connections under cyclic loading, Eng. Struct. 174 (2018) 49-66.
950 [56] J. Li, X. Ren, Stochastic damage model for concrete based on energy equivalent strain, Int. J.
951 Solids Struct. 46(11) (2009) 2407-2419.
952 [57] J.Y. Wu, J. Li, R. Faria, An energy release rate-based plastic-damage model for concrete, Int. J.
953 Solids Struct. 43(3) (2006) 583-612.
954 [58] D. Feng, J. Li, Stochastic nonlinear behavior of reinforced concrete frames. II: Numerical
955 simulation, J. Struct. Eng. 142(3) (2016) 04015163.
956 [59] R. Faria, J. Oliver, M. Cervera, A strain-based plastic viscous-damage model for massive
957 concrete structures, Int. J. Solids Struct. 35(14) (1998) 1533-1558.
958 [60] J. Wu, Damage energy release rate-based elastoplastic damage constitutive model for concrete
959 and its application to nonlinear analysis of structures [Ph.D. thesis], Department of Building
960 Engineering, Tongji University, Tongji University, Shanghai, 2004.
961 [61] R. Shamass, X. Zhou, G. Alfano, Finite-element analysis of shear-off failure of keyed dry joints
962 in precast concrete segmental bridges, J. Bridge Eng. 20(6) (2015) 04014084.
963 [62] F. Faleschini, P. Bragolusi, M.A. Zanini, P. Zampieri, C. Pellegrino, Experimental and numerical
964 investigation on the cyclic behavior of RC beam column joints with EAF slag concrete, Eng. Struct.
965 152 (2017) 335-347.
966 [63] X. Lv, Z. Yu, Z. Shan, Seismic behaviour of frame structures with assembly of prefabricated
967 concrete beam, J. Build. Eng. 40 (2021) 102765.
968 [64] W. Huang, G. Hu, X. Miao, Z. Fan, Seismic performance analysis of a novel demountable precast
969 concrete beam-column connection with multi-slit devices, J. Build. Eng. 44 (2021) 102663.
970 [65] A. Hanaor, A. Ben-Arroyo, Prestressed bolting in precast concrete beam-column connection,
971 Proceedings of the institution of civil engineers: Structures and buildings, Thomas Telford Services
972 Ltd, 1998, pp. 144-153.
973